Article

Developmental Cell

A hydraulic feedback loop between mesendoderm cell migration and interstitial fluid relocalization promotes embryonic axis formation in zebrafish

Graphical abstract

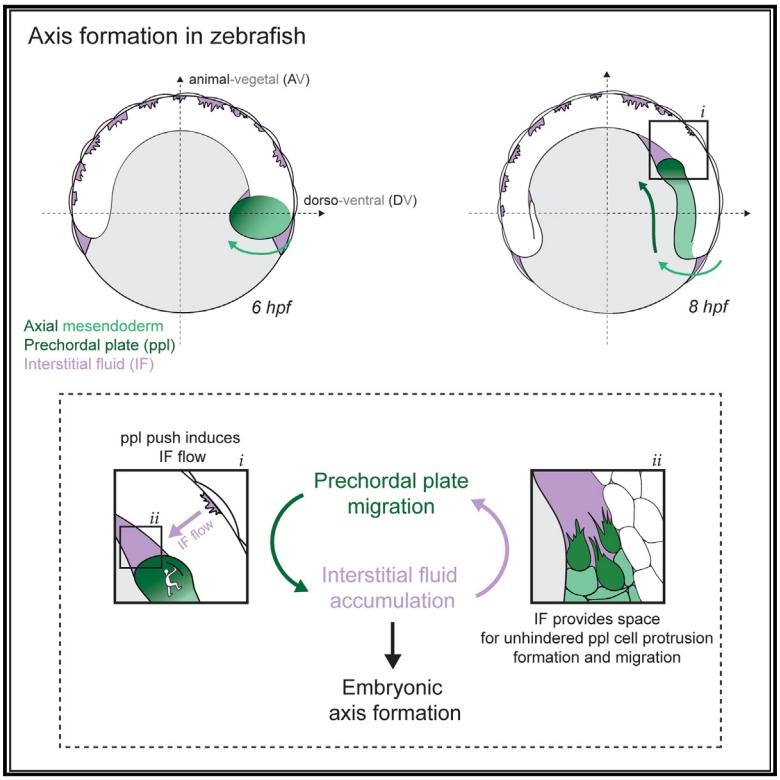

Authors

Karla Huljev, Shayan Shamipour, Diana Pinheiro, ..., Christoph Markus Sommer, Suyash Naik, Carl-Philipp Heisenberg

Correspondence

heisenberg@ist.ac.at

In brief

Huljev et al. show how interstitial fluid functions in mesendoderm cell migration during zebrafish gastrulation: mesendoderm migration, by pushing against the overlying blastoderm, triggers interstitial fluid accumulation at its front. This interstitial fluid accumulation, in turn, facilitates mesendoderm migration by providing the space for unhindered protrusion formation.

Highlights

- Axial mesendoderm migration triggers IF accumulation at its front
- IF accumulation provides the space needed for unhindered axial mesendoderm migration
- Advancing mesendoderm exerts pushing forces on the overlying deep cell layer
- These pushing forces cause IF flow through the deep cell layer to the mesendoderm front

Huljev et al., 2023, Developmental Cell *58*, 582–596
April 10, 2023
https://doi.org/10.1016/j.devcel.2023.02.016

CellPress

CellPress
OPEN ACCESS

Developmental Cell

Article

A hydraulic feedback loop between mesendoderm cell migration and interstitial fluid relocalization promotes embryonic axis formation in zebrafish

Karla Huljev,[1] Shayan Shamipour,[2] Diana Pinheiro,[3] Friedrich Preusser,[4] Irene Steccari,[1] Christoph Markus Sommer,[1] Suyash Naik,[1] and Carl-Philipp Heisenberg[1,5,*]

[1]Institute of Science and Technology Austria (ISTA), Klosterneuburg, Austria
[2]Department of Molecular Life Sciences, University of Zurich, Zurich, Switzerland
[3]Research Institute of Molecular Pathology, Vienna Biocenter, 1030 Vienna, Austria
[4]Berlin Institute for Medical Systems Biology (BIMSB), Max Delbrück centre for Molecular Medicine in the Helmholtz Association (MDC), 13125 Berlin, Germany
[5]Lead contact
*Correspondence: heisenberg@ist.ac.at
https://doi.org/10.1016/j.devcel.2023.02.016

SUMMARY

Interstitial fluid (IF) accumulation between embryonic cells is thought to be important for embryo patterning and morphogenesis. Here, we identify a positive mechanical feedback loop between cell migration and IF relocalization and find that it promotes embryonic axis formation during zebrafish gastrulation. We show that anterior axial mesendoderm (prechordal plate [ppl]) cells, moving in between the yolk cell and deep cell tissue to extend the embryonic axis, compress the overlying deep cell layer, thereby causing IF to flow from the deep cell layer to the boundary between the yolk cell and the deep cell layer, directly ahead of the advancing ppl. This IF relocalization, in turn, facilitates ppl cell protrusion formation and migration by opening up the space into which the ppl moves and, thereby, the ability of the ppl to trigger IF relocalization by pushing against the overlying deep cell layer. Thus, embryonic axis formation relies on a hydraulic feedback loop between cell migration and IF relocalization.

INTRODUCTION

Interstitial fluid (IF) accumulations are commonly observed in early embryonic tissue. In some species, such as mice, these accumulations eventually coalesce into a large central lumen, the blastocoel,[1,2] during blastula stages, while in others, such as zebrafish, they remain as small interstitial gaps distributed over the embryo.[3,4] The function of IF accumulations in embryogenesis has only begun to be elucidated. Recent studies in mice have suggested that long-distance fluid exchange between hundreds of micron-sized lumina within the blastoderm leads to the formation of a single dominant lumen, the forming blastocoel, and that this process is important for initial embryo symmetry breaking.[2] Furthermore, the expansion of the blastocoel in mice, driven by an increase in luminal pressure, has been proposed to promote junction maturation between trophectoderm cells lining the blastocoel, thereby helping trophectoderm cells to sustain increased pressure within the blastocoel.[1]

The mouse blastocoel has also been suggested to function as a source of morphogen signaling, influencing cell-fate specification in the surrounding cells. The release of fibroblast growth factor 4 (FGF4) into the mouse blastocoel influences epiblast-to-primitive-endoderm lineage segregation within the inner cell mass during blastocyst development by promoting endoderm differentiation in cells of the inner cell mass facing the cavity.[5] Likewise, deposition of bone morphogenetic protein (BMP) into the pro-amniotic cavity, another large fluid-filled cavity forming in the early mouse embryo, together with its diffusion through narrow interstitial channels, plays a critical role in the formation of a robust BMP signaling gradient within the early mouse embryo.[6]

Although these findings point to an important role of IF accumulations and their coalescence into large fluid-filled cavities for embryo patterning and differentiation, comparably little is known about whether and how IF accumulations also function in the processes by which the embryo takes shape. Gastrulation, when the different germ layers—ectoderm, mesoderm, and endoderm—are formed within the embryo, is typically accompanied by characteristic and large-scale reorganization of IF accumulations. These dynamic changes in IF accumulations are likely important for germ layer formation, as evidenced, for instance, by studies on chick and sea urchin gastrulation, where the blastocoel appears to act as a vessel into which the individual mesoderm cells ingress, thereby facilitating embryo stratification.[7,8] Furthermore, in frog gastrulation, intrablastocoelic hydrostatic pressure promotes fibronectin matrix assembly on the

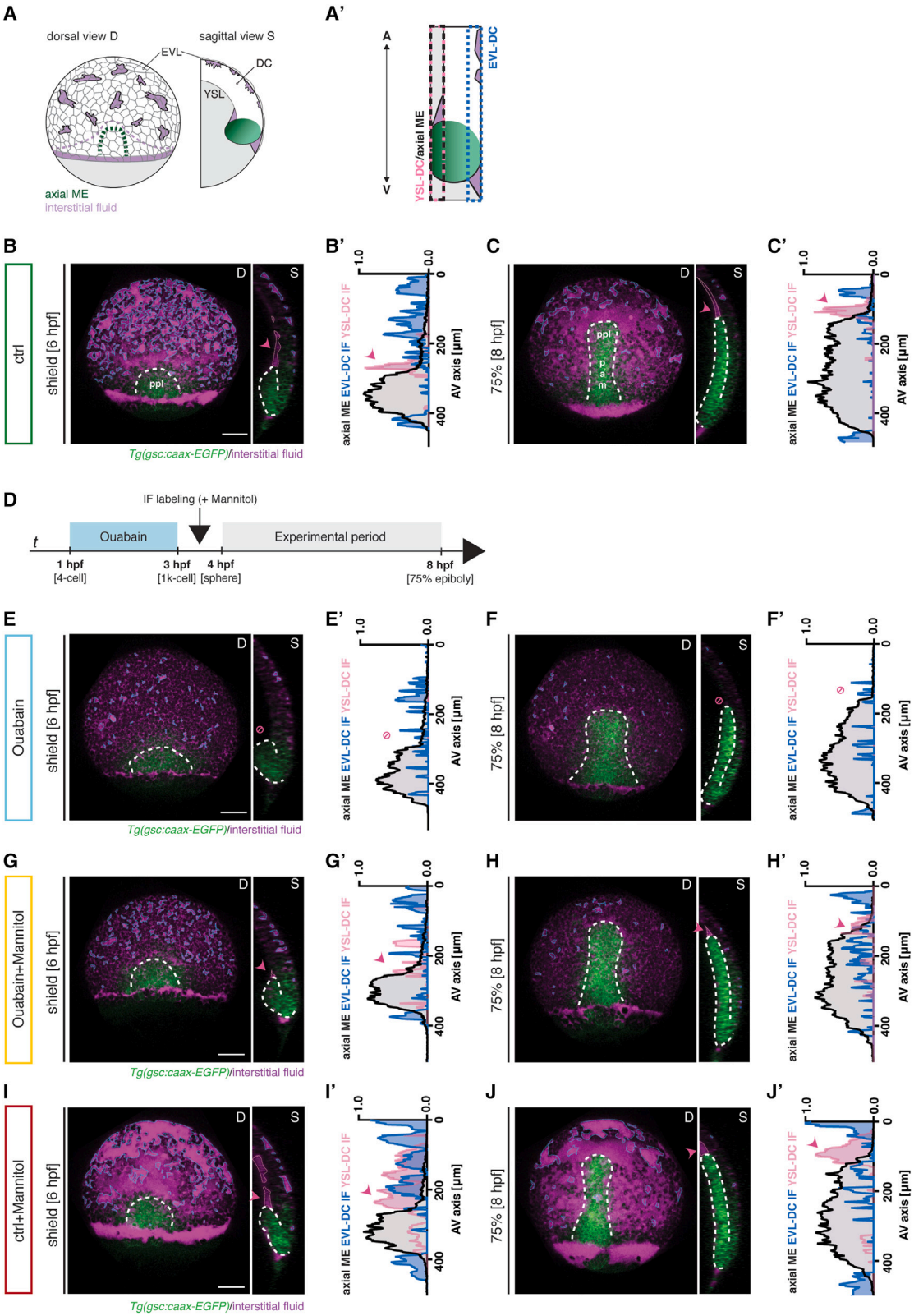

(legend on next page)

blastocoel roof, forming the substrate for mesoderm migration.[9] During subsequent stages of frog gastrulation, a second fluid-filled cavity, the gastrocoel or archenteron, emerges, by accumulating IF at the expense of the shrinking blastocoel.[10] This redistribution of IF between the two cavities coincides with the internalized head-mesoderm at the blastocoel roof undergoing convergence movements, leading to its compaction and stiffening, a process important for neural crest cell migration.[11] Yet, while these different findings suggest a potential function of IF accumulations in regulating cell migration during gastrulation, direct evidence supporting such function is still sparse.

In zebrafish, IF accumulations during early blastula stages are widely distributed among the deep cells (DCs) within the blastoderm.[3,4] However, unlike in other vertebrates, these accumulations do not coalesce into a large central cavity and, consequently, no clearly recognizable blastocoel is formed at the onset of gastrulation.[4] Interestingly, recent studies have shown that cultured zebrafish blastoderm explants lacking the yolk cell are capable of forming a blastocoel, suggesting that the association of the blastoderm with the yolk cell interferes with blastocoel formation within the embryo.[3,12,13] Yet, whether IF accumulations, and their dynamic redistribution, play any role in zebrafish gastrulation is still unknown.

RESULTS

IF relocalization coincides with axial mesendoderm internalization and migration

To investigate the potential role of IF accumulations within the blastoderm during zebrafish gastrulation, we first systematically determined how the distribution of IF changes during this period. At pre-gastrula stages (4–6 h post fertilization [hpf]), IF localization gradually changed from an initially even distribution of fluid-filled gaps between DCs to a preferential accumulation of IF at the boundary between the enveloping layer (EVL) at the surface of the blastoderm and the DCs underneath (named 'EVL-DC boundary' hereafter; 3.5–6 hpf; Figures S1A–S1D). This was followed by spatiotemporally highly coordinated relocalization of IF from the EVL-DC boundary to the boundary between the DCs and the underlying yolk syncytial layer (YSL) (named 'YSL-DC boundary' hereafter; 6–8 hpf; Figures S1A–S1D). Notably, this relocalization became first apparent at the blastoderm/germ ring margin at the time when mesendoderm progenitors began internalizing there (6 hpf, Figures 1A–1B′; Video S1), and then spread from the margin to the animal pole of the blastoderm, concomitant with the animal pole-directed migration of mesendoderm progenitors (Figures 1C and 1C′; Video S1).

To test whether there might be a correlation between the relocalization of IF from the EVL-DC to the YSL-DC boundary, and the concomitant internalization and animal-directed migration of mesendoderm progenitors, we analyzed to what extent these different events are spatiotemporally coordinated. The accumulation of IF at the YSL-DC boundary closely correlated in both space and time with the disappearance of IF from the EVL-DC boundary and the appearance of mesendoderm progenitors migrating along the YSL-DC boundary toward the animal pole (Figures 1A–1C′; Video S1). Importantly, this highly orchestrated relocalization of IF was most clearly recognizable at the dorsal side of the gastrula (Figures 1A–1C′; Video S1), where a compact cluster of anterior axial mesendoderm (prechordal plate [ppl]) progenitors, closely followed by highly cohesive posterior axial mesendoderm progenitors, internalizes and migrates in a straight path toward the animal pole.[14–17] In lateral and ventral regions of the gastrula, in contrast, where mesendoderm progenitors internalize and migrate as more loosely aggregated cells,[18] the relocalization of IF was much less pronounced (Figures S1E and S1E′). Moreover, analyzing the total amount of IF within the blastoderm during its relocalization did not show any major changes in IF volume (Figures S1F–S1G′), suggesting that this relocalization represents a redistribution of IF within the blastoderm rather than *de novo* accumulation at the YSL-DC boundary. Collectively, these findings point to the possibility that there might be a functional link between the relocalization of IF from the EVL-DC to YSL-DC boundary with the internalization and animal-directed migration of ppl progenitors at the onset of gastrulation.

Extracellular osmolarity controls the amount of IF accumulation within the blastoderm

To address the functional relevance of the IF accumulation at the YSL-DC boundary for ppl progenitor cell migration, we sought to interfere with the overall IF accumulation within the blastoderm and analyze how this affects ppl cell migration. To this end, we asked how IF accumulation is regulated within the blastoderm.

Figure 1. Interstitial fluid accumulation requires Na^+/K^+-ATPase activity and relocalizes during axial mesendoderm internalization and migration

(A) Schematic of interstitial fluid (IF) distribution during axial mesendoderm (ME) internalization at 6 h post fertilization (hpf); D, dorsal and S, sagittal views; EVL, enveloping layer; DC, deep cell; YSL, yolk syncytial layer. (A′) Schematic illustrating the principle of IF relocalization analysis at the dorsal side; AV, animal-vegetal axis; pink and blue rectangles indicate the regions of IF accumulation analysis at the YSL-DC and EVL-DC boundaries, respectively, during axial ME internalization and migration (black rectangle).

(B, C, and E–J) Maximum intensity projections (D, dorsal view) and single cross-sections (S, sagittal view) of *gsc::caax-EGFP* embryos expressing EGFP within the axial ME and injected with fluorescent dextran to mark IF in control (B and C), ouabain-treated (E and F), ouabain-treated and mannitol-injected (G and H), and mannitol-injected (I and J) embryos at 6 hpf (B, E, G, and I), and 8 hpf (C, F, H, and J); dashed white lines outline the anterior axial mesendoderm/prechordal plate (ppl) and, due to the leaky nature of this transgenic reporter line, also the posterior axial ME (pam); dashed blue lines outline the IF at the EVL-DC boundary; dashed pink lines outline the IF at the YSL-DC boundary (S, sagittal view); scale bars, 100 μm. (B′, C′, and E′–J′) IF distribution profiles along the AV axis relative to the position of ppl/pam, marked by *gsc::caax-EGFP* expression (black lines), in control (green, B′ and C′), ouabain-treated (blue, E′ and F′), ouabain-treated and mannitol-injected (yellow, G′ and H′), and mannitol-injected (red, I′ and J′) embryos at 6 hpf (B′, E′, G′, and I′) and 8 hpf (C′, F′, H′, and J′); multi-color curves represent average values of n = 3 independent embryo replicates of the position of ppl/pam (black lines) and IF distribution at the EVL-DC (blue lines) and YSL-DC (pink lines) boundaries; arrowheads (pink) indicate the IF accumulation ahead of the ppl.

(D) Schematic illustrating the experimental design. Control and ouabain-treated (1 mM, 1–3 hpf) embryos were injected with fluorescent dextran (to mark the IF) either alone or in combination with mannitol (400 mM).

See also Figures S1 and S2 and Videos S1 and S2.

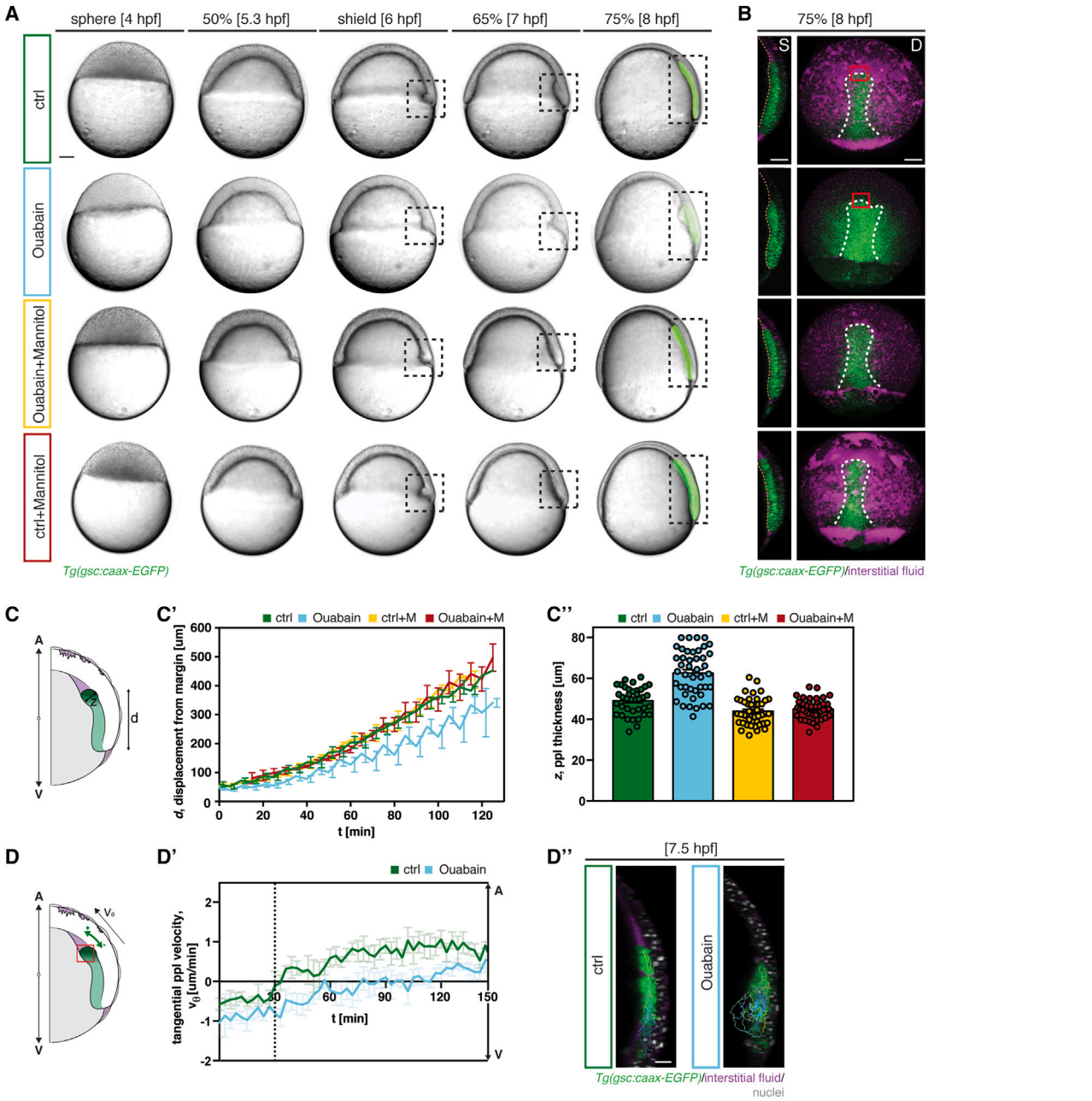

(legend on next page)

The first accumulations of IF within the blastoderm became apparent at early cleavage stages (32- to 64-cell stage, Figures S2A–S2B′), when cleavage orientation changes[19] and cells at the blastoderm surface polarize along their apicobasal axis (Figure S2C). Surface cell polarization and IF accumulation were accompanied by the restricted localization of Na^+/K^+-ATPases, key regulators of IF accumulation in other organisms[20,21] to the basolateral side of surface cells (Figure S2C′), pointing at the possibility that Na^+/K^+-ATPases are involved in IF accumulation within the blastoderm. To test this possibility, we transiently blocked Na^+/K^+-ATPase activity at the onset of IF formation by exposing embryos to 1 mM of the specific Na^+/K^+-ATPase inhibitor, ouabain,[1,5] from 1 to 3 hpf (Figure 1D). Treated embryos showed strongly reduced IF accumulation within the blastoderm from the beginning of IF formation in control embryos (64- to 128-cell stage, Figure S2D) to the end of gastrulation (Figures S2J and S2K). This reduced accumulation of IF was accompanied by a transient swelling of the blastoderm cells (Figure S2E), which, however, normalized before the onset of gastrulation movements (Figures S2F and S2G). Reduced IF accumulations in ouabain-treated embryos displayed the same overall pattern of dynamic relocalization as found in control embryos, first to the boundary between EVL and DCs and then from there to the YSL-DC boundary, although in strongly affected embryos this was often hardly recognizable (Figures 1E–1F′, S2J, and S2K; Video S2). This suggests that ouabain treatment predominantly interferes with IF accumulation per se, but not necessarily with the processes regulating its relocalization within the blastoderm.

To determine whether Na^+/K^+-ATPases function in IF accumulation by regulating intra- to extracellular fluid osmolarity, as found in other organisms,[20,21] we injected mannitol (36.4 ng/embryo) into the extracellular space of ouabain-treated embryos at 3.5 hpf to increase extracellular osmolarity. Mannitol injection partially rescued the overall IF accumulation in ouabain-treated embryos, thereby restoring the characteristic accumulation ahead of the ppl (Figures 1G–1H′, S2L, and S2M; Video S2). This suggests that ouabain inhibits IF accumulation within the blastoderm by changing the ratio of extra- to intracellular osmolarity. Consistently, injection of mannitol into the extracellular space of 3.5-hpf control embryos increased the total amount of IF above the level typically found in control embryos but did not abolish the general pattern of IF relocalization observed in control embryos, except for some minor level of premature IF relocalization to the YSL-DC boundary in mannitol-injected embryos (Figures 1I–1J′, S2N, and S2O; Video S2). Together, these findings suggest that regulating extracellular osmolarity represents an effective tool for tuning the amount of IF accumulation in early blastula and gastrula stage embryos.

IF accumulation is required for ppl cell protrusion formation and migration

Being able to modulate IF accumulation within the blastoderm, we next asked whether IF accumulation in front of the advancing ppl progenitors is needed for their migration toward the animal pole of the gastrula. Embryos transiently exposed to 1 mM ouabain from 1 to 3 hpf to block IF accumulation within the blastoderm showed a pronounced thickening of the dorsal germ ring at the position where the embryonic shield forms[15] (Figures 2A–2C and 2C″; Video S2), while doming and epiboly movements appeared normal (Figures S3A and S3A′). This local thickening of the germ ring/shield was due to internalizing ppl progenitors failing to migrate away from the germ ring margin and, consequently, piling up at the margin where internalization occurs (Figures 2C, 2C′, and S2P; Video S2). In line with this, tracking ppl progenitors in ouabain-treated embryos showed slower animal pole-directed movements of internalized ppl progenitors when compared with untreated control embryos (Figures 2D–2D″; Video S2). Internalization movements of ppl progenitors in ouabain-treated embryos, in contrast, did not display any clearly detectable defects (Figures S3B and S3B′). To test whether this failure in ppl progenitor cell migration is due to ouabain blocking

Figure 2. Interstitial fluid accumulation is required for prechordal plate cell migration

(A) Bright-field and fluorescence (8 h post fertilization, hpf) images of control (green), ouabain-treated (blue), ouabain-treated and mannitol-injected (yellow), and mannitol-injected (red) *gsc::caax-EGFP* embryos expressing EGFP within the prechordal plate (ppl)/posterior axial mesendoderm (pam) from 4 to 8 hpf; dashed boxed region marks the zone of ppl internalization; dorsal to the right; scale bars, 100 μm.

(B) Single cross-sections (S, sagittal view) and maximum intensity projections (D, dorsal view) of control (green), ouabain-treated (blue), ouabain-treated and mannitol-injected (yellow), and mannitol-injected (red) *gsc::caax-EGFP* embryos expressing EGFP within the ppl/pam at 8 hpf; dashed orange lines outline the yolk syncytial layer (YSL)-deep cell (DC) boundary (S, sagittal view); dashed white lines outline the ppl/pam (D, dorsal view); scale bars, 100 μm.

(C) Schematic illustrating the principle of ppl distance from the margin (C′) and thickness (C″) quantification. (C′) Distance of the ppl leading edge to the germ ring margin as a function of developmental time after the onset of internalization (6 hpf, corresponding to 0′) for control (green, n = 9), ouabain-treated (blue, n = 9), ouabain-treated and mannitol-injected (yellow, n = 6), and mannitol-injected embryos (red, n = 4); mean ± SEM. (C″) Ppl thickness from 6 to 8 hpf in control (green, n = 4), ouabain-treated (blue, n = 4), ouabain-treated and mannitol-injected (yellow, n = 4), and mannitol-injected embryos (red, n = 4); mean ± SEM.

(D) Schematic illustrating the principle of ppl animal-directed velocity quantification; AV, animal-vegetal axis. (D′) Animal-directed velocities of individual ppl cells in control (green, n = 5) and ouabain-treated embryos (blue, n = 4); mean ± SEM. (D″) Representative three-dimensional ppl cell tracks (7.5 hpf) in control (green) and ouabain-treated (blue) *gsc::caax-EGFP* embryos at 7.5 hpf; sagittal views.

(E) High resolution images of the ppl leading edge (dorsal view; red boxed region in B) in control (green) and ouabain-treated (blue) *gsc::caax-EGFP* transgenic embryos expressing EGFP within the ppl/pam at the onset (10′) and progression (30′) of ppl migration; interstitial fluid (IF) and YSL were labeled by injection of fluorescent dextrans to gain contrast; arrowheads/inserts show the extension of an exemplary filopodium (f), bleb (b), and lamellipodium (l) in the direction of migration; scale bars, 20 μm.

(F) Quantification of normalized ppl leading edge length in control (green, n = 3) and ouabain-treated (blue, n = 3) embryos; dashed black line marks the detachment of the DCs from the YSL and onset of IF accumulation.

(G) Number of lamellipodia, filopodia, and blebs per time frame, normalized for the number of cells in control (green, n = 3) and ouabain-treated (blue, n = 3) embryos; individually plotted values represent protrusion numbers per minute and cell; mean ± SEM; Mann-Whitney test. n, number of independent embryo replicates.

See also Figure S3 and Video S2.

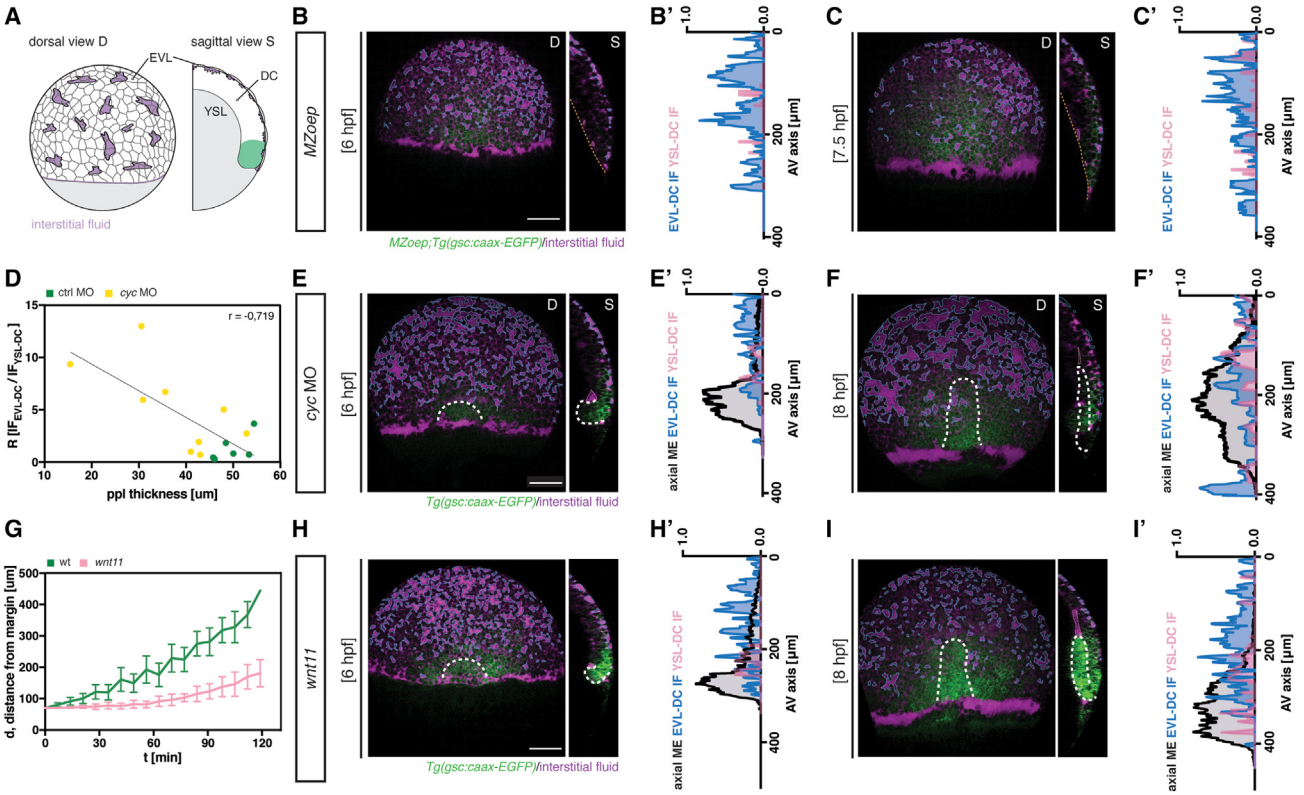

Figure 3. Axial mesendoderm internalization is required for efficient interstitial fluid relocalization

(A) Schematic of interstitial fluid (IF) distribution at 6 h post fertilization (hpf) (onset of prechordal plate [ppl] internalization in wild-type [WT] embryos) in *MZoep*;*gsc::caax-EGFP* embryos; D, dorsal and S, sagittal views; EVL, enveloping layer; DC, deep cell; YSL, yolk syncytial layer.

(B, C, E, F, H, and I) Maximum intensity projections (D, dorsal view) and single cross-sections (S, sagittal view) of *MZoep* (B and C), *cyc* morphant (MO, 4 ng) (E and F), and *slb/wnt11f2* (H and I) *gsc::caax-EGFP* embryos at 6 hpf (B, E, and H) and 8 hpf (C, F, and I); for control embryos see (Figures 1B and 1C); dashed orange lines outline the YSL-DC boundary (S, sagittal view) in *MZoep* embryos; dashed white lines outline the ppl and, due to the leaky nature of this transgenic reporter line, also the posterior axial mesendoderm (pam); dashed blue lines outline the IF at the EVL-DC boundary; dashed pink lines outline the IF at the YSL-DC boundary (S, sagittal view); scale bars, 100 μm. (B′, C′, E′, F′, H′, and I′) IF distribution profiles along the animal-vegetal (AV) axis in *MZoep* mutant (B′ and C′), *cyc* MO (E′ and F′), and *slb/wnt11f2* (H′ and I′) embryos relative to the position of ppl/pam, as indicated by *gsc::caax-EGFP* expression at 6 hpf (B′, E′, and H′) and 8 hpf (C′, F′, and I′); multi-color curves represent average values of n = 3 independent embryo replicates of the position of ppl/pam (black lines) and IF distribution at the EVL-DC (blue lines) and YSL-DC (pink lines) boundaries.

(D) Correlation between IF relocalization and ppl thickness in control (green, n = 5) and *cyc* MO embryos (yellow, n = 4). Pearson correlation coefficient (r) is shown.

(G) Distance of the ppl transplant leading edge from the germ ring margin as a function of developmental time (6 hpf, corresponding to 0′) in WT (green, n = 10) and *slb/wnt11f2* (pink, n = 11) *gsc::caax-EGFP* embryos; mean ± SEM. n, number of independent embryo replicates.

See also Figure S4.

IF accumulation within the blastoderm, we partially restored IF accumulation by injecting mannitol into the extracellular space in ouabain-treated embryos. Mannitol injection not only effectively restored IF accumulation ahead of the advancing ppl progenitors (Figures 1G–1H′; Video S2) but also their migration away from the germ ring margin toward the animal pole (Figures 2C–2C″; Video S2). In contrast, increasing IF accumulations within the blastoderm above control levels by injecting mannitol in untreated control embryos had no recognizable effect on germ ring morphology or ppl progenitor cell migration (Figures 2C–2C″; Video S2). Finally, to strengthen the functional link between IF accumulation and ppl cell migration, we sought to interfere with IF accumulation within the blastoderm by blocking Na^+/K^+-ATPase activity through drugs other than ouabain and then determine whether such reduction in IF accumulation would also lead to defects in ppl cell migration. We found that treating embryos with 10 μM digitoxin, a specific inhibitor of Na^+/K^+-ATPase activity,[22] not only led to strongly reduced IF accumulation but also diminished animal-pole-directed ppl cell migration (Figures S3F–S3J), thereby closely phenocopying the effects observed after ouabain treatment. Collectively, these findings suggest that IF accumulation in front of the internalized ppl has a permissive function, facilitating ppl cell migration toward the animal pole.

To understand why IF accumulation ahead of the advancing ppl progenitors is required for normal ppl progenitor cell migration, we analyzed ppl progenitor cell morphology and movement in ouabain-treated versus control embryos. Once internalized, cells at the leading edge of the ppl migrate toward the animal pole using the YSL as a substrate for their migration and forming various types of cell protrusions, including lamellipodia, filopodia, and blebs that adhere to the YSL by Cadherin-1 (Cdh1)-mediated

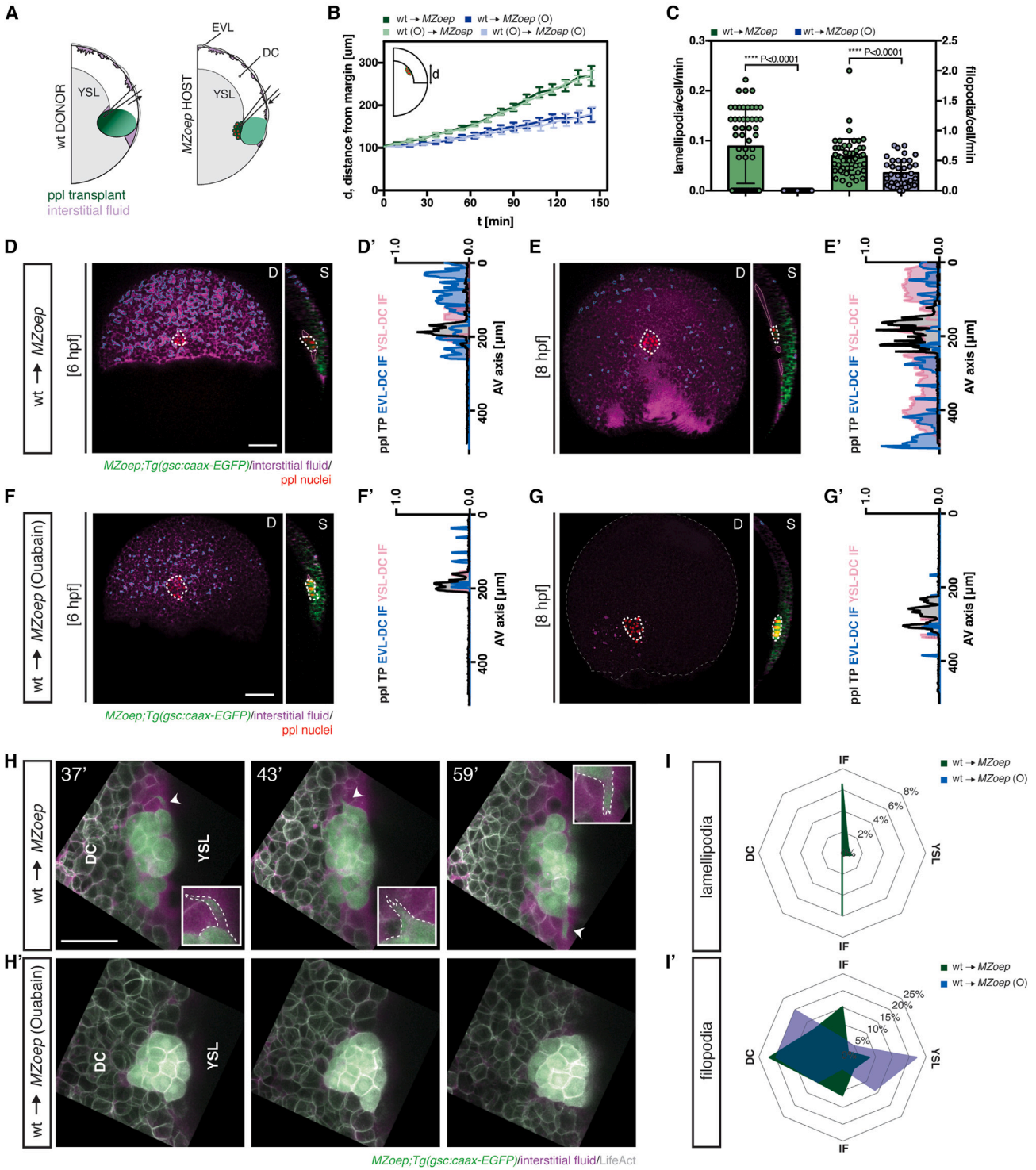

Figure 4. Prechordal plate migration is sufficient for interstitial fluid relocalization

(A) Schematic of interstitial fluid (IF) distribution at 6 h post fertilization (hpf) (onset of prechordal plate [ppl] internalization in wild-type [WT] embryos) in *MZoep gsc::caax-EGFP* embryos containing transplanted ppl cells; D, dorsal and S, sagittal views; EVL, enveloping layer; DC, deep cell; YSL, yolk syncytial layer.

(B) Distance of the ppl transplant leading edge from the germ margin as a function of developmental time (6 hpf, corresponding to 0′) in control (green, n = 6) and ouabain (O)-treated (blue, n = 9) *MZoep;gsc::caax-EGFP* host embryos containing untreated ppl cells, and control (light green, n = 4) and ouabain-treated (light blue, n = 2) *MZoep;gsc::caax-EGFP* host embryos containing ouabain-treated ppl cells; N, number of independent embryo replicates; schematic of distance measurements in upper left corner; mean ± SEM.

(legend continued on next page)

cell-cell adhesion[14,23] (Figures 3D and 3F). Extracellular matrix accumulation at the YSL-DC boundary, in contrast, only becomes detectable at later stages of gastrulation[24] and thus is unlikely to be directly involved in ppl cell migration. Protrusion formation in ppl cells closely coincided with the accumulation of IF in front of the internalized ppl (Figures 3D–3G), and was strongly reduced in ouabain-treated embryos with blocked IF accumulation within the blastoderm (Figures 3D–3G). To test whether this reduction of ppl cell protrusion formation in ouabain-treated embryos was due to ouabain blocking IF accumulations and not other potentially more direct effects of ouabain on ppl cell migration and/or protrusion formation, we plated induced anterior axial mesendoderm cells on fibronectin-coated substrates and analyzed whether ouabain would affect protrusion-driven mesendoderm cell spreading. No significant difference in cell spreading capacity could be detected between treated and control cells (Figures S3C–S3D), suggesting that ouabain does not directly interfere with anterior axial mesendoderm cell protrusion formation and spreading. Finally, to exclude that ouabain treatment interferes with ppl cell migration by affecting ppl cell-fate specification, we analyzed the expression of *hatching gland gene* (*hgg*), a characteristic marker gene of ppl cell-fate specification,[25] in ouabain-treated and control embryos. The expression of *hgg* remained largely unchanged in ouabain-treated embryos (Figure S3E), indicating that ouabain does not affect ppl cell migration by interfering with ppl cell-fate specification. Collectively, these results suggest that the accumulation of IF in front of the advancing ppl facilitates ppl cell migration by promoting cell protrusion formation.

IF relocalization requires ppl cell migration

Next, we asked whether not only IF relocalization facilitates ppl cell migration but also whether ppl migration feeds back on IF relocalization. For testing this hypothesis, we determined whether IF relocalization would occur when ppl progenitor cell internalization and animal-directed migration are impaired. To this end, we first turned to maternal-zygotic *one-eyed pinhead* mutant embryos (*MZoep*), which are defective in mesendoderm specification and germ layer formation.[26] In *MZoep* mutants, IF largely remained at the EVL-DC boundary, and only small IF fragments appeared at the YSL-DC boundary at the time (6–7.5 hpf; Figures 3A–3C′) when IF relocalization was observed in wild-type (WT) embryos or *MZoep* mutants rescued by injection of *oep* mRNA (Figures 1A–1C′ and S4A–S4B′). At later stages of gastrulation (7–8 hpf), IF relocalization was also observed in *MZoep* mutants; however, different from WT embryos, this relocalization simultaneously occurred in most of the blastoderm except its margin (Figure S4C). This suggests that mesendoderm internalization and migration are required for timely and spatially coordinated IF relocalization at the onset of gastrulation.

To further test whether the amount and migratory activity of internalized mesendoderm determine the extent of IF relocalization, we analyzed IF relocalization in *cyclops* (*cyc*) morphant embryos, where the number of ppl progenitors, and thus the size of the ppl, is reduced at varying degrees,[27,28] and in *slb/wnt11* mutant embryos, where the advancement of ppl cells toward the animal pole is diminished.[25] In *cyc* morphant embryos, IF relocalization from the EVL-DC to the YSL-DC boundary ahead of the ppl leading edge was still detectable (6–8 hpf; Figures 3E–3F′). However, the extent by which this relocalization occurred was greatly diminished, closely matching the variable reduction in the size of the ppl found in *cyc* morphant embryos (Figure 3D), suggesting that the size of the ppl determines the extent of IF relocalization. Furthermore, in *slb/wnt11* mutant embryos, reduced animal-pole-directed migration of ppl cells was accompanied by a reduction in the progressive relocalization of IF from the EVL-DC to the YSL-DC boundary and a less pronounced accumulation of IF ahead of the advancing ppl (Figures 3G–3I′; for control see Figures 1B–1C′), suggesting that the migration of ppl cells is required for progressive IF relocalization.

Ppl internalization and migration are sufficient to trigger IF relocalization

To determine whether ppl cell internalization and migration are not only required but also sufficient for IF relocalization from the EVL-DC to the YSL-DC boundary, we sought to rescue IF relocalization in *MZoep* mutant embryos by transplanting a cluster of ppl cells (~15–20 cells) from a WT donor embryo to the YSL-DC boundary close to the germ margin of an *MZoep* host embryo at 5.7 hpf (Figure 4A). In transplanted *MZoep* embryos, IF accumulated at the YSL-DC boundary surrounding the transplanted ppl cell cluster at 6 hpf (shield stage in WT embryos), accompanied by a local depletion from the EVL-DC boundary directly above the transplanted cluster (Figures 4D–4E′; Video S3). This

(C) Number of lamellipodia and filopodia per time frame, normalized for the number of cells, in ppl cells taken from *gsc::caax-EGFP* donor embryos injected with *LifeAct-RFP* mRNA (50 pg) and transplanted into control (green, n = 3) and ouabain-treated (blue, n = 3) *MZoep;gsc::caax-EGFP* host embryos; individually plotted values represent protrusion numbers per minute and cell; mean ± SEM; Mann-Whitney test.
(D–G) Maximum intensity projections (D, dorsal view) and single cross-sections (S, sagittal view) of *MZoep* (D and E) and ouabain-treated *MZoep* (F and G) *gsc::caax-EGFP* embryos containing transplanted ppl cells at 6 (D and F) and 8 hpf (E and G); for control embryos see Figures 1B and 1C; dashed white lines outline the ppl transplant; dashed blue lines outline the IF at the EVL-DC boundary (S, sagittal view); dashed pink lines outline the IF at the YSL-DC boundary (S, sagittal view); scale bars, 100 μm. (D′–G′) IF distribution profiles along the animal-vegetal (AV) axis relative to the position of ppl transplant, as indicated by *gsc::caax-EGFP* expression, in *MZoep* (D′ and E′) and ouabain-treated *MZoep* (F′ and G′) *gsc::caax-EGFP* embryos containing transplanted ppl cells at 6 (D′ and F′) and 8 hpf (E′ and G′); multi-color curves represent average values of n = 3 independent embryo replicates of the position of ppl/pam (black lines) and IF distribution at the EVL-DC (blue lines) and YSL-DC (pink lines) boundaries.
(H) High resolution images of ppl cells taken from *gsc::caax-EGFP* donor embryos injected with *LifeAct-RFP* mRNA (50 pg) and transplanted into control and ouabain-treated *MZoep;gsc::caax-EGFP* host embryos injected with fluorescent dextran to label the IF at different times after transplantation (37′, 43′, and 59′, with 0′ corresponding to 6 hpf); arrowheads/inserts show the extension of an exemplary lamellipodium toward contact-free, IF-filled space; scale bars, 50 μm.
(I,I′) Orientation of lamellipodia (I) and filopodia (I′) per time frame, normalized for the number of ppl cells, taken from *gsc::caax-EGFP* donor embryos injected with *LifeAct-RFP* mRNA (50 pg) and transplanted into control (green, n = 3) and ouabain-treated (blue, n = 3) *MZoep;gsc::caax-EGFP* host embryos injected with fluorescent dextran to label the IF. n, number of independent embryo replicates.
See also Figure S4 and Video S3.

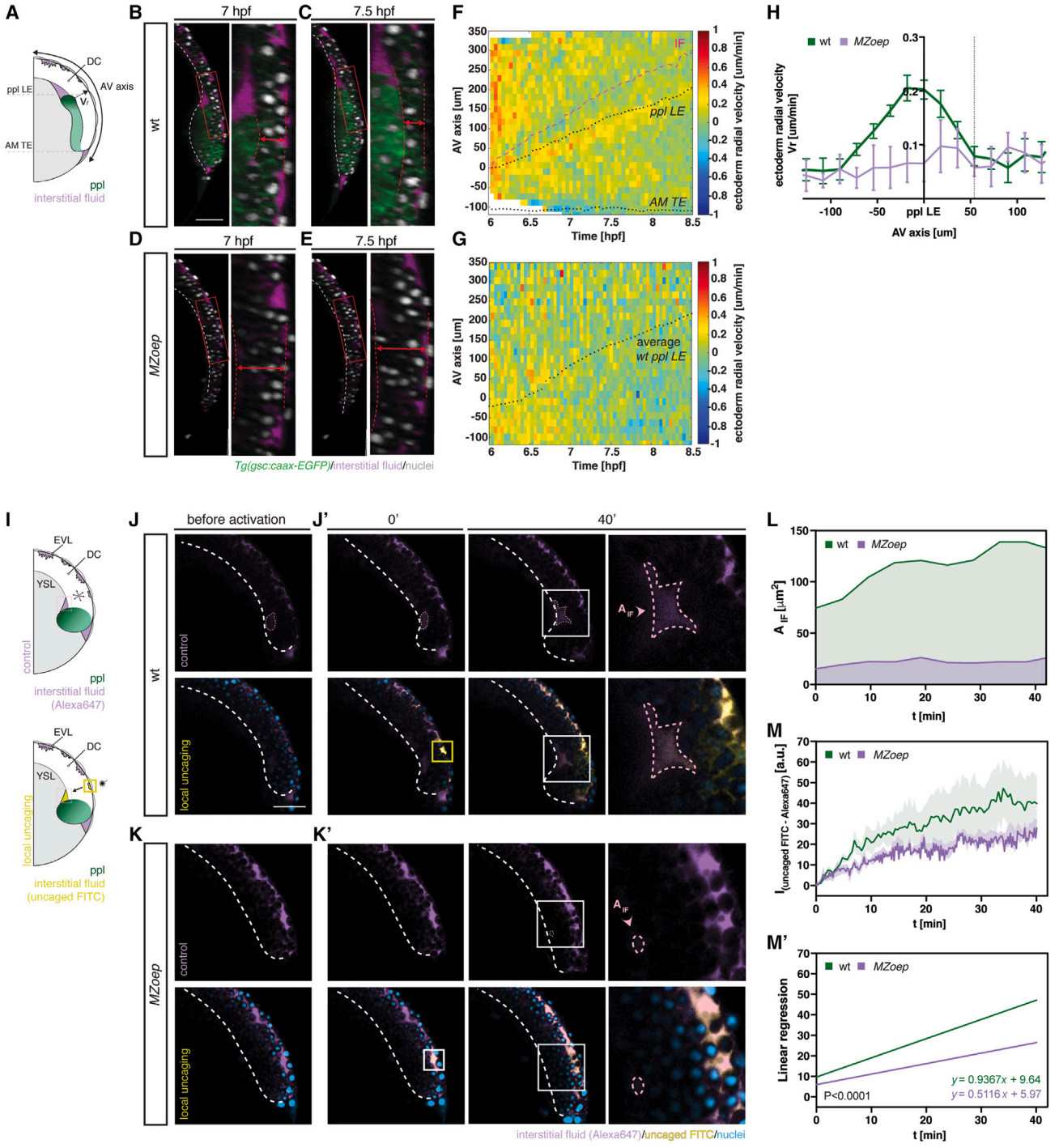

Figure 5. Prechordal plate migration triggers interstitial fluid relocalization by pushing against the overlying epiblast

(A) Schematic of deep cell (DC) radial velocity (V_r) analysis relative to the prechordal plate (ppl) position; ppl leading edge (LE); axial mesendoderm trailing edge (AM TE); animal-vegetal (AV) axis.

(B–E) Representative cross-sections (right panel, close-up on the DC region marked by the red box in the left panel) in *gsc::caax-EGFP* wild-type (WT) (B and C) and *MZoep* (D and E) embryos at 7 (B and D) and 7.5 hpf (C and E); dashed white line outlines the yolk syncytial layer (YSL)-DC boundary; dashed red line outlines the deformation of the DC tissue relative to the ppl position; scale bars, 100 μm.

(F and G) Representative heatmaps of DC radial displacement along the AV axis as a function of developmental time in *gsc::caax-EGFP* WT (F) and *MZoep* (G) embryos; dotted black lines mark the position of the ppl LE (top) and the position of AM TE (bottom); dashed magenta line indicates the position of the interstitial fluid (IF) ahead of the ppl LE; in (G), the position of ppl LE was superimposed from an average value of ppl position in WT embryos; DC radial velocities are color-coded.

(legend continued on next page)

is different from the situation in WT embryos, where IF predominantly accumulated ahead of the migrating ppl due to the presence of more posterior axial mesoderm progenitors behind the ppl in these embryos, obstructing IF accumulation there (Figures 4E and 4E′; Video S3). Notably, the transplanted ppl cell cluster, while being uniformly surrounded by IF at the YSL-DC boundary, still displayed directed migration away from the germ margin toward the animal pole (Figure 4B; Video S3), leading to a progressive relocalization of IF from the EVL-DC to the YSL-DC boundary along the path of their migration (Figures 4E and 4E′; Video S3). This progressive relocalization was slowed down when migratory defective *slb/wnt11* ppl cells were transplanted into *slb/wnt11 morpholino*-injected *MZoep* host embryos (Figures S4H–S4L), supporting the notion that ppl cell migration triggers this relocalization. Collectively, these findings suggest that ppl cell internalization and migration are sufficient to trigger IF relocalization from the EVL-DC to the YSL-DC boundary, but also that this relocalization does not provide positional cues required for directed ppl cell migration.

To further test whether IF accumulation around the cluster is required for animal pole-directed ppl cell migration, as found in WT embryos, we inhibited IF accumulation in host *MZoep* embryos by transiently exposing them to 1 mM ouabain during IF formation (1–3 hpf). When a ppl cell cluster from an untreated WT embryo was transplanted to the YSL-DC boundary of an ouabain-treated *MZoep* embryo, no clear IF relocalization to the YSL-DC boundary around the transplanted cell cluster was observed from shield to mid-gastrulation stages (6–8 hpf; Figures 4F–4G′; Video S3). This lack of proper IF relocalization was accompanied by the transplanted ppl cells failing to efficiently migrate away from the germ margin toward the animal pole (Figure 4B; Video S3). To exclude that the inability of ppl cells to undergo directed migration in ouabain-treated *MZoep* embryos is not due to ouabain directly affecting the migratory capability of the transplanted ppl cells, we asked whether ppl cells can undergo directed migration when transplanted from an ouabain-treated WT donor embryo into an untreated *MZoep* host embryo. We found that ppl clusters from ouabain-treated donors not only properly accumulated IF at the YSL-DC boundary surrounding them (Figures S4D–S4E′) but also migrated toward the animal pole similar to non-treated transplanted ppl cells (Figure 4B). In contrast, when ppl cells from ouabain-treated donors were transplanted into ouabain-treated *MZoep* hosts, IF relocalization failed (Figures S4F–S4G′) and the transplanted cells did not display directed migration toward the animal pole (Figure 4B). Together, this suggests that IF relocalization is required for normal ppl cell migration toward the animal pole.

Finally, to determine whether the inability of transplanted ppl cells in ouabain-treated *MZoep* host embryos to undergo directed migration was due to defective IF relocalization to the YSL-DC boundary affecting their protrusion formation, as found in ouabain-treated WT embryos (Figures 2E–2G), we analyzed protrusion formation of the transplanted cells. Although ppl cells transplanted into untreated *MZoep* host embryos formed both lamellipodia and filopodia along the YSL-DC boundary, preferentially oriented in the direction of their migration toward the animal pole, the formation of such oriented protrusions was strongly diminished in ppl cells transplanted into ouabain-treated *MZoep* embryos lacking IF relocalization (Figures 4C and 4H–4I′). This suggests that, similar to the situation in ouabain-treated WT embryos, defective IF relocalization in ouabain-treated *MZoep* host embryos interferes with the directed migration of transplanted ppl cells by impairing protrusion formation in these cells.

Ppl triggers IF relocalization from the EVL-DC to the YSL-DC boundary by pushing against the overlying epiblast

Our finding that the ppl triggers IF relocalization from the EVL-DC to the YSL-DC boundary, raises questions as to the mechanism(s) by which this highly orchestrated IF relocalization is achieved. One possibility is that the ppl, by squeezing in between the DC layer and YSL, pushes the overlying DC layer (epiblast) outward against the EVL, thereby triggering an opposite-directed inward flow of IF from the EVL-DC boundary through the DC layer to the YSL-DC boundary. To challenge this hypothesis, we first asked whether the advancing ppl indeed pushes against the overlying epiblast by analyzing the extent of DC movements along the radial axis of the epiblast adjacent to the ppl (Figures 5A–5H; Video S4). We detected a pronounced outward radial movement of DCs above the ppl, which led to DC compaction above the ppl and gradually propagated in the direction of the animal pole as the ppl was moving in the same direction (Figures 5A–5C, 5F, and 5H; Video S4). These progressive outward radial movement and compaction of DCs were also accompanied by an indentation of the YSL/yolk cell directly below the advancing ppl (Figures S5A–S5C), consistent with the ppl squeezing in between the DC layer and YSL, thereby deforming them. To further challenge this hypothesis, we turned to *MZoep* mutants lacking ppl and, consequently, timely IF accumulation

(H) Average DC radial velocities relative to the ppl LE position in *gsc::caax-EGFP* WT (n = 4) and *MZoep* (n = 3) embryos; dashed line at ~50 μm indicates the maximum position along the AV axis at which ppl-mediated radial DC movements are still detectable of the ppl LE; mean ± SEM.
(I) Schematic of IF distribution visualized by a uniformly distributed control dye (top panel) and local ultraviolet (UV) laser photoactivation/uncaging of a caged dye within the IF at the enveloping layer (EVL)-DC boundary, ahead and above of the internalizing ppl (yellow square), and detection of the uncaged dye at the YSL-DC boundary (pink dashed square), ahead of the advancing ppl (bottom panel).
(J–K′) Representative cross-sections of *gsc::caax-EGFP* WT (J and J′) and *MZoep* (K and K′) embryos before (50% epiboly; J and K) and after UV laser activation (0′ and 40′, J′ and K′); panels on the right in (J′) and (K′) are close-up views of the indicated regions in the left panels (40′) with dashed pink lines outlining the growing IF accumulation at the YSL-DC boundary, where the accumulation of uncaged-FITC was quantified; top row, control dye (Alexa647) uniformly marking the IF; bottom row, uncaged-FITC distribution; yellow squares mark the UV laser activation site; dashed white lines outline the YSL-DC boundary; scale bars, 100 μm.
(L–M′) IF accumulation area at the YSL-DC boundary ahead of the ppl (L), and corresponding accumulation of uncaged-FITC within that region (M and M′) in *gsc::caax-EGFP* WT (green area; green line; n = 4) and *MZoep* (purple area; purple line; n = 4) embryos as a function of time after the onset of internalization (6 hpf) at 0′; values represent the mean. n, number of independent embryo replicates. See also Figure S5 and Videos S4 and S5.

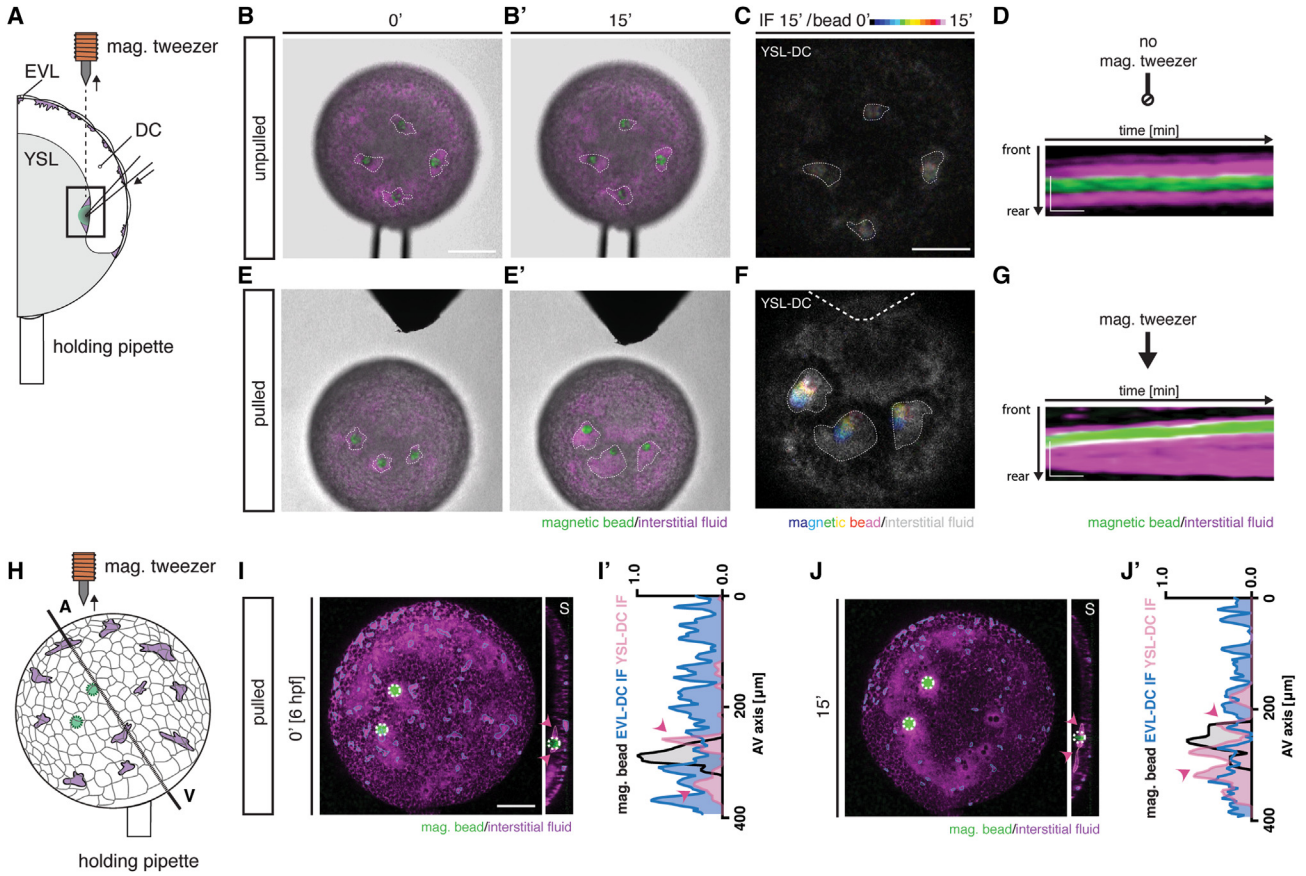

Figure 6. Magnetic bead pulling induces interstitial fluid accumulation at the yolk syncytial layer-deep cell boundary

(A) Schematic of mechanical induction of interstitial fluid (IF) relocalization by a controlled displacement of a magnetic bead, implanted at the YSL (yolk syncytial layer)-deep cell (DC) boundary of an *MZoep* embryo, using a focused magnetic field; embryo was held by a blunt micropipette (d = 80 μm); EVL, enveloping layer.

(B, B′, E, and E′) Representative cross-sections of the magnetic tweezer experiments with unpulled (B and B′) and pulled magnetic beads (E and E′) at the start of the experiment (B and E) and 15′ later (B′ and E′); dashed white line outlines the IF accumulation at the YSL-DC boundary; scale bars, 200 μm.

(C and F) Representative cross-section images of non-pulled (C) and pulled (F) magnetic beads at the YSL-DC boundary where the trajectory of bead movement is projected over a period of 15′; time is color-coded; dashed white line marks the position of the magnetic tweezer; scale bars, 250 μm.

(D and G) Representative kymographs of IF accumulation relative to the position of the magnetic bead, either unpulled (D) or pulled (G), via a focused magnetic field.

(H) Schematic illustrating the embryo orientation during IF relocalization by a controlled displacement of a magnetic bead, implanted at the YSL-DC boundary of an *MZoep* embryo; AV, animal-vegetal axis.

(I and J) Maximum intensity projections and single cross-sections (S, sagittal view) of *MZoep;gsc::caax-EGFP* embryos injected with fluorescent dextran to mark IF during mechanical induction of interstitial fluid (IF) at the beginning of the experiment (I) and 15′ after the pull (J); dashed white circles outline implanted magnetic beads; dashed blue lines outline the IF at the EVL-DC boundary; dashed pink lines outline the IF at the YSL-DC boundary (sagittal view, S); scale bars, 100 μm.

(I′ and J′) IF distribution profiles along the axis of controlled displacement of a magnetic bead at the beginning of the experiment (I′) and 15′ after the pull (J′); multicolor curves represent average values of n = 3 independent embryo replicates of the position of magnetic bead (black lines) and IF distribution at the EVL-DC (blue lines) and YSL-DC (pink lines) boundaries; arrowheads (pink) indicate the IF accumulation ahead of the ppl.

See also Video S6.

at the YSL-DC boundary[26] (Figures 3A–3C′). No clearly recognizable radial movement and compaction of DCs and yolk cell indentation were detected in *MZoep* embryos (Figures 5D, 5E, 5G, 5H, and S5A–S5C; Video S4), further supporting the notion that these processes depend on ppl moving in between the DC layer (epiblast) and YSL toward the animal pole.

For pushing forces originating from the advancing ppl triggering an opposite-directed inward flow of IF from the EVL-DC boundary through the DC layer to the YSL-DC boundary, the DC layer ahead of the advancing ppl must remain sufficiently porous to allow for such flows to happen. To address this requirement, we analyzed DC-layer compaction ahead of the ppl during ppl cell migration (Figures S5D and S5E). We found that, while the DC layer directly above the ppl clearly underwent compaction, the DC layer ahead of the ppl remained loosely packed with many small pockets of IF accumulations (Figure S5E), compatible with the possibility of IF flowing through this layer.

To monitor whether the IF indeed flows through the DC layer from the EVL-DC to YSL-DC boundary, we injected a photoactivatable dye (DMNB [dimethoxynitrobenzyl]-caged fluorescein) into the IF and locally uncaged it with an ultraviolet (UV)

laser at the EVL-DC boundary ahead of the migrating ppl at the onset of internalization (Figure 5I). We then followed the redistribution of these locally photoactivated fluorescent tracers during ppl animal pole-directed migration (Figures 5J and S5F; Video S5). As a control, we performed the same experiment in *MZoep* mutant embryos lacking ppl specification/migration and proper IF relocalization[26] (Figures 3A–3C′ and S5F′). With the onset of ppl internalization and animal pole-directed migration in WT embryos, the photoactivated fluorescent tracer relocalized from its source of generation at the EVL-DC boundary to the place of IF accumulation at the YSL-DC boundary directly ahead of the migrating ppl (Figures 5J, 5J′, and 5L; Video S5). This relocalization was not solely due to simple diffusion of the uncaged dye from its source of generation, as the rate of uncaged dye accumulation at the YSL-DC boundary was clearly higher in WT embryos as compared with *MZoep* mutants lacking ppl and IF relocalization (Figures 5K, 5K′, 5L–5M′, S5C, and S5D; α_{WT} = 0.9367 > α_{MZoep} = 0.5116; Video S5). Together, these findings support the notion that IF flows from the EVL-DC to the YSL-DC boundary as a result of ppl internalization and migration.

Finally, we asked whether pushing by the ppl against the overlying DC layer (epiblast) would be sufficient to trigger IF relocalization. To this end, we transplanted a passivated and fluorescently labeled magnetic bead, roughly the same size as the anterior ppl (d = 40 μm), into the YSL-DC boundary of *MZoep* mutant embryos and determined whether pulling the bead along this boundary would trigger IF relocalization from the EVL-DC to the YSL-DC boundary (Figure 6A). Strikingly, we found that IF accumulated at the YSL-DC boundary around the transplanted bead, both for control (unpulled) beads and beads that we subsequently pulled using a magnet, and that this IF accumulation around the transplanted bead at the YSL-DC boundary was accompanied by a reduction of IF above the bead at the EVL-DC boundary (Figures 6B–6J′; Video S6). Moreover, pulling the bead along the YSL-DC boundary led to a progressive IF relocalization from the EVL-DC to the YSL-DC boundary along its movement path, which persisted for several minutes (Figures 6E–6J′; Video S6), consistent with the notion that mechanically pushing against the overlying DC layer (epiblast) is sufficient to trigger progressive and persistent IF relocalization from the EVL-DC to the YSL-DC boundary. To further challenge this model, we sought to trigger ectopic IF relocalization in relocalization-defective *MZoep* mutant embryos by applying local pushing forces from the outside on the EVL. Locally pushing on the EVL of *MZoep* mutants using a micropipette led to a partial relocalization of IF from the EVL-DC to the YSL-DC boundary (Figures S6A–S6D), suggesting that such pushing forces are sufficient to trigger this relocalization.

Collectively, these observations suggest that the ppl, by moving in between the YSL and epiblast, pushes against the overlying epiblast, leading to IF flowing from the EVL-DC to the YSL-DC boundary just ahead of the ppl, which in turn promotes ppl cell migration.

DISCUSSION

Recent work in mouse embryos has suggested that IF accumulation within the forming blastocoel/pro-amniotic cavity can affect cell-fate specification and differentiation by exerting mechanical forces on the surrounding tissues and/or functioning as signaling hubs.[1,5,6] Our findings in zebrafish, in contrast, point to a predominantly morphogenetic function of localized IF accumulation ahead of the advancing ppl in providing sufficient space for unhindered ppl cell protrusion formation and directed migration. This not only identifies a yet unknown function of IF accumulation in embryo morphogenesis but also points to apparent differences in the developmental function of IF accumulation between zebrafish and mice. These different roles of IF accumulations in controlling cell-fate specification in mice versus cell migration in zebrafish could be due to mouse, but not zebrafish, embryos forming a large blastocoel/pro-amniotic cavity, which exposes the blastoderm-lining cells to a large fluid interface, affecting their fate specification through biochemical signaling and mechanosensation.[1,5] Further analysis of IF accumulation in other blastocoel forming and non-forming species will be needed to elucidate the origin of the functional diversification of IF accumulation in early embryogenesis.

Mechanistically, we propose that a hydraulic feedback loop between ppl cell migration and IF accumulation is achieved by the migrating ppl pushing against the overlying DC layer (epiblast), thereby building up a pressure gradient that triggers IF flow and relocalization ahead of the advancing ppl. This IF accumulation, again, promotes ppl cell migration by opening up the space required for unhindered cell migration. Ppl progenitors have previously been shown to migrate in between DCs and the YSL, using the YSL as a substrate for their migration.[29] Moreover, friction with the overlying DC layer has been shown to slow down directed ppl cell migration,[29] suggesting that the contact between ppl cells and the overlying DC layer constrains ppl cell migration. Consequently, IF accumulating at the YSL-epiblast boundary will likely have an effect on ppl cell migration by simply removing physical obstacles hindering ppl cell migration. This notion is also supported by our observation that defective ppl cell migration in embryos with reduced IF accumulation can be fully rescued simply by increasing osmotic pressure and, as a result, IF accumulation, arguing against a specific function of IF in providing biochemical cues promoting ppl cell protrusion formation and migration.

An important component of the proposed positive hydraulic feedback loop is the function of ppl cell migration in triggering IF relocalization by pushing against the overlying non-internalizing DC layer (epiblast). For this to happen, pushing forces from the advancing ppl must be efficiently transmitted from the ppl to the EVL-DC boundary, and, in response to this pushing force, IF must be able to flow through the DC layer from the EVL-DC to the YSL-DC boundary. This requires the epiblast above the ppl being sufficiently rigid to allow forces being efficiently transmitted from the ppl to the YSL-DC boundary, and the DC layer ahead of the advancing ppl being sufficiently loose and porous for allowing IF to flow through. Such dual properties of the epiblast are likely to be achieved by the ppl triggering the compaction of the overlying DCs and thus enhancing DC tissue rigidity above the ppl, while ahead of the ppl the DCs would remain sufficiently loose and porous for IF to flow through (Figures 5A–5C, 5F, 5H, S5A, and S5B; Video S4). Interestingly, the distribution of IF accumulations has previously been shown to reflect cell connectivity and, as a result, tissue rigidity within

the zebrafish blastoderm.[30] It is thus conceivable that compaction of the DC layer above the ppl leads to an increase in tissue connectivity and, consequently, rigidity, which again would facilitate the transmission of forces from the advancing ppl to the EVL-DC boundary. Yet, how DC compaction translates into specific changes in tissue rigidity and porosity still needs to be investigated.

Cell migration in non-confluent tissue not only involves dynamic changes in cell-cell and cell-matrix contacts but also the reorganization of IF accumulations within the tissue. Our finding of migrating cells self-organizing the physical space required for their unhindered migration by driving large-scale IF flow and relocalization within the embryo, unravels a simple and universally applicable mechanism by which cells can migrate within the spatial confinement of non-confluent tissues.

Limitations of the study

In this study, we show that IF accumulation ahead of the advancing ppl is required for ppl cell protrusion formation and migration, suggesting that IF functions in ppl cell migration by facilitating cell protrusion formation. Although this is a likely scenario, given the functional interdependence between cell protrusion formation and migration, we have not yet addressed the potential contribution of other and/or additional mechanisms by which IF accumulation facilitates ppl cell migration, e.g., by modulating tissue rigidity through an increase in hydrostatic pressure. We also show that pushing forces from the ppl can trigger IF flow from the EVL-DC boundary to the YSL-DC boundary ahead of the ppl. Although such mechanisms would, in principle, be sufficient to explain IF accumulation ahead of the advancing ppl, there might be other potential mechanisms, such as changes in IF osmolarity due to pushing forces by the ppl modulating mechanosensitive ion channels in adjacent DCs, the contribution of which still needs to be addressed in the future by using *in vivo* sensors for IF osmolarity.

STAR★METHODS

Detailed methods are provided in the online version of this paper and include the following:

SUPPLEMENTAL INFORMATION

Supplemental information can be found online at https://doi.org/10.1016/j.devcel.2023.02.016.

ACKNOWLEDGMENTS

We thank Andrea Pauli (IMP) and Edouard Hannezo (ISTA) for fruitful discussions and support with the SPIM experiments; the Heisenberg group, and especially Feyza Nur Arslan and Alexandra Schauer, for discussions and feedback; Michaela Jović (ISTA) for help with the quantitative real-time PCR protocol; the bioimaging and zebrafish facilities of ISTA for continuous support; Stephan Preibisch (Janelia Research Campus) for support with the SPIM data analysis; and Nobuhiro Nakamura (Tokyo Institute of Technology) for sharing α_1-Na^+/K^+-ATPase antibody. This work was supported by funding from the European Union (European Research Council Advanced grant 742573 to C.-P.H.), postdoctoral fellowships from EMBO (LTF-850-2017) and HFSP (LT000429/2018-L2) to D.P., and a PhD fellowship from the Studienstiftung des deutschen Volkes to F.P.

AUTHOR CONTRIBUTIONS

K.H. and C.-P.H. designed the research. K.H. performed most of the experiments and analyzed the experimental data. S.S., C.M.S., and F.P. contributed to data analysis. D.P. performed the ppl transplantation experiments and I.S. performed the quantitative real-time PCR experiments. S.N. performed and analyzed the micropipette-pushing experiments. K.H. and C.-P.H. wrote the manuscript.

DECLARATION OF INTERESTS

C.-P.H. is a member of the editorial board of *Developmental Cell*.

Received: January 10, 2022
Revised: August 31, 2022
Accepted: February 20, 2023
Published: March 16, 2023

REFERENCES

1. Chan, C.J., Costanzo, M., Ruiz-Herrero, T., Mönke, G., Petrie, R.J., Bergert, M., Diz-Muñoz, A., Mahadevan, L., and Hiiragi, T. (2019). Hydraulic control of mammalian embryo size and cell fate. Nature *571*, 112–116. https://doi.org/10.1038/s41586-019-1309-x.
2. Dumortier, J.G., Le Verge-Serandour, M., Tortorelli, A.F., Mielke, A., de Plater, L., Turlier, H., and Maître, J.L. (2019). Hydraulic fracturing and active coarsening position the lumen of the mouse blastocyst. Science *365*, 465–468. https://doi.org/10.1126/science.aaw7709.
3. Krens, S.F.G., Veldhuis, J.H., Barone, V., Čapek, D., Maître, J.L., Brodland, G.W., and Heisenberg, C.P. (2017). Interstitial fluid osmolarity modulates the action of differential tissue surface tension in progenitor

cell segregation during gastrulation. Development *144*, 1798–1806. https://doi.org/10.1242/dev.144964.

4. Petridou, N.I., Grigolon, S., Salbreux, G., Hannezo, E., and Heisenberg, C.P. (2019). Fluidization-mediated tissue spreading by mitotic cell rounding and non-canonical Wnt signalling. Nat. Cell Biol. *21*, 169–178. https://doi.org/10.1038/s41556-018-0247-4.
5. Ryan, A.Q., Chan, C.J., Graner, F., and Hiiragi, T. (2019). Lumen expansion facilitates epiblast-primitive endoderm fate specification during mouse blastocyst formation. Dev. Cell *51*, 684–697.e4. https://doi.org/10.1016/j.devcel.2019.10.011.
6. Zhang, Z., Zwick, S., Loew, E., Grimley, J.S., and Ramanathan, S. (2019). Mouse embryo geometry drives formation of robust signaling gradients through receptor localization. Nat. Commun. *10*, 4516. https://doi.org/10.1038/s41467-019-12533-7.
7. Kominami, T., and Takata, H. (2004). Gastrulation in the sea urchin embryo: a model system for analyzing the morphogenesis of a monolayered epithelium. Dev. Growth Differ. *46*, 309–326. https://doi.org/10.1111/j.1440-169x.2004.00755.x.
8. Voiculescu, O. (2020). Movements of chick gastrulation. Curr. Top. Dev. Biol. *136*, 409–428. https://doi.org/10.1016/bs.ctdb.2019.11.015.
9. Dzamba, B.J., Jakab, K.R., Marsden, M., Schwartz, M.A., and DeSimone, D.W. (2009). Cadherin adhesion, tissue tension, and noncanonical Wnt signaling regulate fibronectin matrix organization. Dev. Cell *16*, 421–432. https://doi.org/10.1016/j.devcel.2009.01.008.
10. Ewald, A.J., Peyrot, S.M., Tyszka, J.M., Fraser, S.E., and Wallingford, J.B. (2004). Regional requirements for Dishevelled signaling during Xenopus gastrulation: separable effects on blastopore closure, mesendoderm internalization and archenteron formation. Development *131*, 6195–6209. https://doi.org/10.1242/dev.01542.
11. Barriga, E.H., Franze, K., Charras, G., and Mayor, R. (2018). Tissue stiffening coordinates morphogenesis by triggering collective cell migration in vivo. Nature *554*, 523–527. https://doi.org/10.1038/nature25742.
12. Fulton, T., Trivedi, V., Attardi, A., Anlas, K., Dingare, C., Arias, A.M., and Steventon, B. (2020). Axis specification in zebrafish is robust to cell mixing and reveals a regulation of pattern formation by morphogenesis. Curr. Biol. *30*, 2984–2994.e3. https://doi.org/10.1016/j.cub.2020.05.048.
13. Schauer, A., Pinheiro, D., Hauschild, R., and Heisenberg, C.P. (2020). Zebrafish embryonic explants undergo genetically encoded self-assembly. eLife *9*, e55190. https://doi.org/10.7554/eLife.55190.
14. Montero, J.A., Kilian, B., Chan, J., Bayliss, P.E., and Heisenberg, C.P. (2003). Phosphoinositide 3-kinase is required for process outgrowth and cell polarization of gastrulating mesendodermal cells. Curr. Biol. *13*, 1279–1289. https://doi.org/10.1016/s0960-9822(03)00505-0.
15. Montero, J.A., Carvalho, L., Wilsch-Bräuninger, M., Kilian, B., Mustafa, C., and Heisenberg, C.P. (2005). Shield formation at the onset of zebrafish gastrulation. Development *132*, 1187–1198. https://doi.org/10.1242/dev.01667.
16. Keller, P.J., Schmidt, A.D., Wittbrodt, J., and Stelzer, E.H. (2008). Reconstruction of zebrafish early embryonic development by scanned light sheet microscopy. Science *322*, 1065–1069. https://doi.org/10.1126/science.1162493.
17. Dumortier, J.G., Martin, S., Meyer, D., Rosa, F.M., and David, N.B. (2012). Collective mesendoderm migration relies on an intrinsic directionality signal transmitted through cell contacts. Proc. Natl. Acad. Sci. USA *109*, 16945–16950. https://doi.org/10.1073/pnas.1205870109.
18. Myers, D.C., Sepich, D.S., and Solnica-Krezel, L. (2002). Bmp activity gradient regulates convergent extension during zebrafish gastrulation. Dev. Biol. *243*, 81–98. https://doi.org/10.1006/dbio.2001.0523.
19. Olivier, N., Luengo-Oroz, M.A., Duloquin, L., Faure, E., Savy, T., Veilleux, I., Solinas, X., Débarre, D., Bourgine, P., Santos, A., et al. (2010). Cell lineage reconstruction of early zebrafish embryos using label-free nonlinear microscopy. Science *329*, 967–971. https://doi.org/10.1126/science.1189428.
20. Slack, C., and Warner, A.E. (1973). Intracellular and intercellular potentials in the early amphibian embryo. J. Physiol. *232*, 313–330. https://doi.org/10.1113/jphysiol.1973.sp010272.
21. Marikawa, Y., and Alarcon, V.B. (2012). Creation of trophectoderm, the first epithelium, in mouse preimplantation development. Results Probl. Cell Differ. *55*, 165–184. https://doi.org/10.1007/978-3-642-30406-4_9.
22. Sun, Y., Dong, Z., Khodabakhsh, H., Chatterjee, S., and Guo, S. (2012). Zebrafish chemical screening reveals the impairment of dopaminergic neuronal survival by cardiac glycosides. PLoS One *7*, e35645. https://doi.org/10.1371/journal.pone.0035645.
23. Diz-Muñoz, A., Krieg, M., Bergert, M., Ibarlucea-Benitez, I., Muller, D.J., Paluch, E., and Heisenberg, C.P. (2010). Control of directed cell migration in vivo by membrane-to-cortex attachment. PLoS Biol. *8*, e1000544. https://doi.org/10.1371/journal.pbio.1000544.
24. Latimer, A., and Jessen, J.R. (2010). Extracellular matrix assembly and organization during zebrafish gastrulation. Matrix Biol. *29*, 89–96. https://doi.org/10.1016/j.matbio.2009.10.002.
25. Heisenberg, C.P., Tada, M., Rauch, G.J., Saúde, L., Concha, M.L., Geisler, R., Stemple, D.L., Smith, J.C., and Wilson, S.W. (2000). Silberblick/Wnt11 mediates convergent extension movements during zebrafish gastrulation. Nature *405*, 76–81. https://doi.org/10.1038/35011068.
26. Gritsman, K., Zhang, J., Cheng, S., Heckscher, E., Talbot, W.S., and Schier, A.F. (1999). The EGF-CFC protein one-eyed pinhead is essential for nodal signaling. Cell *97*, 121–132. https://doi.org/10.1016/s0092-8674(00)80720-5.
27. Karlen, S., and Rebagliati, M. (2001). A morpholino phenocopy of the cyclops mutation. Genesis *30*, 126–128. https://doi.org/10.1002/gene.1046.
28. Fan, X., Hagos, E.G., Xu, B., Sias, C., Kawakami, K., Burdine, R.D., and Dougan, S.T. (2007). Nodal signals mediate interactions between the extra-embryonic and embryonic tissues in zebrafish. Dev. Biol. *310*, 363–378. https://doi.org/10.1016/j.ydbio.2007.08.008.
29. Smutny, M., Ákos, Z., Grigolon, S., Shamipour, S., Ruprecht, V., Čapek, D., Behrndt, M., Papusheva, E., Tada, M., Hof, B., et al. (2017). Friction forces position the neural anlage. Nat. Cell Biol. *19*, 306–317. https://doi.org/10.1038/ncb3492.
30. Petridou, N.I., Corominas-Murtra, B., Heisenberg, C.P., and Hannezo, E. (2021). Rigidity percolation uncovers a structural basis for embryonic tissue phase transitions. Cell *184*, 1914–1928.e19. https://doi.org/10.1016/j.cell.2021.02.017.
31. Mistry, A.C., Honda, S., Hirata, T., Kato, A., and Hirose, S. (2001). Eel urea transporter is localized to chloride cells and is salinity dependent. Am. J. Physiol. Regul. Integr. Comp. Physiol. *281*, R1594–R1604. https://doi.org/10.1152/ajpregu.2001.281.5.R1594.
32. Cooper, M.S., Szeto, D.P., Sommers-Herivel, G., Topczewski, J., Solnica-Krezel, L., Kang, H.C., Johnson, I., and Kimelman, D. (2005). Visualizing morphogenesis in transgenic zebrafish embryos using BODIPY TR methyl ester dye as a vital counterstain for GFP. Dev. Dyn. *232*, 359–368. https://doi.org/10.1002/dvdy.20252.
33. Heisenberg, C.P., Brand, M., Jiang, Y.J., Warga, R.M., Beuchle, D., van Eeden, F.J., Furutani-Seiki, M., Granato, M., Haffter, P., Hammerschmidt, M., et al. (1996). Genes involved in forebrain development in the zebrafish, Danio rerio. Development *123*, 191–203. https://doi.org/10.1242/dev.123.1.191.
34. Pinheiro, D., Kardos, R., Hannezo, É., and Heisenberg, C.-P. (2022). Morphogen gradient orchestrates pattern-preserving tissue morphogenesis via motility-driven unjamming. Nat. Phys. *18*, 1482–1493. https://doi.org/10.1038/s41567-022-01787-6.
35. Ruprecht, V., Wieser, S., Callan-Jones, A., Smutny, M., Morita, H., Sako, K., Barone, V., Ritsch-Marte, M., Sixt, M., Voituriez, R., and Heisenberg, C.P. (2015). Cortical contractility triggers a stochastic switch to fast amoeboid cell motility. Cell *160*, 673–685. https://doi.org/10.1016/j.cell.2015.01.008.

36. Iioka, H., Ueno, N., and Kinoshita, N. (2004). Essential role of MARCKS in cortical actin dynamics during gastrulation movements. J. Cell Biol. *164*, 169–174. https://doi.org/10.1083/jcb.200310027.

37. Arboleda-Estudillo, Y., Krieg, M., Stühmer, J., Licata, N.A., Muller, D.J., and Heisenberg, C.P. (2010). Movement directionality in collective migration of germ layer progenitors. Curr. Biol. *20*, 161–169. https://doi.org/10.1016/j.cub.2009.11.036.

38. Behrndt, M., Salbreux, G., Campinho, P., Hauschild, R., Oswald, F., Roensch, J., Grill, S.W., and Heisenberg, C.P. (2012). Forces driving epithelial spreading in zebrafish gastrulation. Science *338*, 257–260. https://doi.org/10.1126/science.1224143.

39. Rebagliati, M.R., Toyama, R., Haffter, P., and Dawid, I.B. (1998). cyclops encodes a nodal-related factor involved in midline signaling. Proc. Natl. Acad. Sci. USA *95*, 9932–9937. https://doi.org/10.1073/pnas.95.17.9932.

40. Zhang, J., Talbot, W.S., and Schier, A.F. (1998). Positional cloning identifies zebrafish one-eyed pinhead as a permissive EGF-related ligand required during gastrulation. Cell *92*, 241–251. https://doi.org/10.1016/s0092-8674(00)80918-6.

41. Schindelin, J., Arganda-Carreras, I., Frise, E., Kaynig, V., Longair, M., Pietzsch, T., Preibisch, S., Rueden, C., Saalfeld, S., Schmid, B., et al. (2012). Fiji: an open-source platform for biological-image analysis. Nat. Methods *9*, 676–682. https://doi.org/10.1038/nmeth.2019.

42. Sommer, C., Straehle, C., Köthe, U., and Hamprecht, F.A. (2011). Ilastik: interactive learning and segmentation toolkit. IEEE International Symposium on Biomedical Imaging: From Nano to Macro. https://doi.org/10.1109/ISBI.2011.5872394.

43. Kimmel, C.B., Ballard, W.W., Kimmel, S.R., Ullmann, B., and Schilling, T.F. (1995). Stages of embryonic development of the zebrafish. Dev. Dyn. *203*, 253–310. https://doi.org/10.1002/aja.1002030302.

44. Westerfield, M. (2000). The Zebrafish Book. A Guide for the Laboratory Use of Zebrafish (Danio rerio), Fourth Edition (University of Oregon Press).

45. Kimmel, R.A., and Meyer, D. (2010). Molecular regulation of pancreas development in zebrafish. Methods Cell Biol. *100*, 261–280. https://doi.org/10.1016/B978-0-12-384892-5.00010-4.

46. Kaufmann, A., Mickoleit, M., Weber, M., and Huisken, J. (2012). Multilayer mounting enables long-term imaging of zebrafish development in a light sheet microscope. Development *139*, 3242–3247. https://doi.org/10.1242/dev.082586.

47. Hörl, D., Rojas Rusak, F., Preusser, F., Tillberg, P., Randel, N., Chhetri, R.K., Cardona, A., Keller, P.J., Harz, H., Leonhardt, H., et al. (2019). BigStitcher: reconstructing high-resolution image datasets of cleared and expanded samples. Nat. Methods *16*, 870–874. https://doi.org/10.1038/s41592-019-0501-0.

STAR★METHODS

KEY RESOURCES TABLE

REAGENT or RESOURCE	SOURCE	IDENTIFIER
Antibodies		
$\alpha 1$-Na^+/K^+-ATPase antibody produced in rabbit	Gift from Dr. Nobuhiro Nakamura, Tokyo Tech; Mistry et al.[31]	N/A
aPKC antibody produced in rabbit	Santa Cruz Biotechnology	Cat# SC-216; RRID: AB_2300359
ß-Catenin antibody produced in mouse	Sigma-Aldrich	Cat# C7207; RRID: AB_476865
ZO-1 antibody (ZO1-1A12) produced in mouse	Thermo Fisher Scientific	Cat# 33-9100; RRID: AB_87181
Alexa Fluor 488 goat anti-rabbit IgG (H+L)	Thermo Fischer Scientific	Cat# A-11008; RRID: AB_143165
Alexa Fluor 647 goat anti-mouse IgG (H+L)	Thermo Fischer Scientific	Cat# A-21235; RRID: AB_2535804
Chemicals, peptides, and recombinant proteins		
Universal agarose	VWR	Cat# 732-2789
Ouabain octahydrate	Sigma-Aldrich	Cat# O3125
Digitoxin	Sigma-Aldrich	Cat# D5878
D-Mannitol	Sigma-Aldrich	Cat# M4125
Dextran, Alexa Fluor™ 647, 10000 MW	Invitrogen	Cat# D22914
Dextran, Tetramethylrhodamine, 10000 MW	Invitrogen	Cat# D1868
Dextran, DMNB-caged fluorescein, 10000 MW	Molecular Probes	Cat# D3310
Dextran, Fluorescein, 10000 MW	Invitrogen	Cat# D1820
Atto 488-Biotin	Sigma-Aldrich	Cat# 30574
Nile Red	Sigma-Aldrich	Cat# 19123
Dulbecco's Modified Eagle Medium/Nutrient Mixture F-12	Sigma-Aldrich	Cat# D6434
Fibronectin bovine plasma	Sigma-Aldrich	Cat# F1141
GlutaMAX™ Supplement	Thermo Fischer Scientific	Cat# 35050061
Critical commercial assays		
mMESSAGE mMACHINE™ SP6 Transcription Kit	Invitrogen	Cat# AM1340
Experimental models: Organisms/strains		
Zebrafish: wildtype ABxTL	MPI-CBG Dresden	N/A
Zebrafish: *Tg(gsc::EGFP-CAAX)*	Smutny et al.[29]	ZFINID:ZDB-ALT-170811-2
Zebrafish: *Tg(actb2::HRAS-EGFP)*	Cooper et al.[32]	ZDB-ALT-061107-2
Zebrafish: *MZ*oep	Gritsman et al.[26]	ZFINID:ZDB-ALT-980203-1256
Zebrafish: *slb/wnt11f2*	Heisenberg et al.[33]	ZDB-GENE-990603-12
Zebrafish: *MZoep;Tg(gsc::EGFP-CAAX)*	Pinhero et al.[34]	ZFINID:ZDB-ALT-980203-1256; ZFINID: ZDB-ALT-170811-2
Zebrafish: *Tg(sebox::EGFP)*	Ruprecht et al.[35]	ZFINID:ZDB-ALT- 150727-1
Oligonucleotides		
Human ß-Globin Morpholino: 5′-CCTCTTAC CTCAGTTACAATTTATA-3′	Gene Tools	N/A
Cyclops Morpholino: 5'-GCGACTCCGAGC GTGTGCATGATG-3′	Gene Tools	N/A
Wnt11f2 Morpholino: 5'-GAAAGTTCCTGT ATTCTGTCATGTC-3′	Gene Tools	N/A
hgg1 forward and reverse primers (5'-CTATTATGAGAGAGCATGTAGCAG - 3' and 5' - CATGTATATGTAGCCTTTGTCAC - 3')	Microsynth	N/A

(*Continued on next page*)

Continued

REAGENT or RESOURCE	SOURCE	IDENTIFIER
ef1α forward and reverse primers (5'-TCTCTCAATCTTGAAACTTAT - 3' and 5' - AACACCCAGGCGTACTTGAA- 3')	Microsynth	N/A
Recombinant DNA		
pCS2-Membrane-RFP	Iioka et al.[36]	N/A
pCS2$^+$-H2A-mCherry	Arboleda-Estudillo et al.[37]	N/A
pCS2$^+$-LifeAct-RFP	Behrndt et al.[38]	N/A
pCS2$^+$-Cyclops	Rebagliati et al.[39]	N/A
pT7-TS-Oep	Zhang et al.[40]	N/A
Software and algorithms		
Fiji	Schindelin et al.[41]	https://fiji.sc/
Imaris (RRID:SCR_007370)	Bitplane	https://imaris.oxinst.com/packages
Excel	Microsoft	https://products.office.com/en-us/?rtc=1
GraphPad Prism	GraphPad Software	https://www.graphpad.com/scientific-software/prism/
MATLAB	MATLAB Software	https://www.mathworks.com/products/matlab.html
Ilastik	Sommer et al.[42]	https://www.ilastik.org/
Illustrator	Adobe	https://www.adobe.com/products/illustrator.html

RESOURCE AVAILABILITY

Lead contact

Further information and requests for resources, reagents, data, and code should be addressed to the lead contact, Carl-Philipp Heisenberg (heisenberg@ist.ac.at), as described in greater detail on our STAR Methods website

Materials availability

This study did not generate new unique reagents.

Data and code availability

There are no new datasets reported in this paper. Code used for image analysis and any additional information required to reanalyze the data reported in this paper are available from the lead contact upon request.

- Imaging data, including raw data, reported in this paper are available from the lead contact upon request.
- Code used for image analysis reported in this paper is available from the lead contact upon request.
- Any additional information required to reanalyze the data reported in this paper is available from the lead contact upon request.

EXPERIMENTAL MODEL AND SUBJECT DETAILS

Fish lines and maintenance

Zebrafish (*Danio rerio*) were housed in 28°C water (pH 7.5 and conductivity 400 μS) with a 14 h on/10 h off light cycle. All zebrafish husbandry was performed under standard conditions according to local regulations, and all procedures were approved by the Ethics Committee of IST Austria regulating animal care and usage. Wild type AB and TL strains, and *Tg(gsc::EGFP-CAAX)*, *Tg(actb2::HRAS-EGFP)*, *MZoep*, *slb/wnt11f2*, and *MZoep;Tg(gsc::EGFP-CAAX)* zebrafish lines were used in this study. Embryos were raised in either E3 medium or Danieau's buffer, kept at 28.5 or 31°C and staged according to Kimmel et al.[43] Fish were bred in the zebrafish facility at IST Austria according to local regulations, and all procedures were approved by the Ethics Committee of IST Austria regulating animal care and usage.

METHOD DETAILS

Dextran, mRNA and Morpholino injections

Embryos were oriented laterally in injection molds and injected with a microinjection needle at 1-cell stage through the yolk cell into the blastoderm.[44] Microinjection needles (30-0020, Harvard Apparatus) were pulled using a P-97 needle puller (Sutter Instruments).

Injections were performed using a microinjection system (PV820, World Precision Instruments). For blastoderm segmentation, the cell cytoplasm was labelled by injection of 1 nl of 1 mg/mL of Dextran-FITC (D1820, Invitrogen) or Dextran Alexa Fluor 647 (D22914, Invitrogen) in wild type (wt) and *MZoep* mutant embryos at the 1-cell stage. For labelling the YSL, 0.5 nL of 1 mg/mL of Dextran TMR (D1868, Invitrogen) was injected into the forming YSL at high stage (3.3 hpf). mRNA transcription was performed using the mMESSAGE mMACHINE Kit (Ambion) and all plasmids used in this study are detailed in the key resources table. The cell nuclei were labelled by injection of 50 pg *H2A-mCherry* mRNA into at 1-cell stage embryos.[37] For labeling cell membranes and cortical actin, 80 pg *membrane-RFP*,[36] 50 pg of *membrane-GFP*,[45] and 50 pg *lifeact-RFP* mRNA were co-injected in 1-cell stage embryos.[38] To generate embryos with smaller prechordal plate (ppl), 4 ng of *cyc morpholino* (MO) (5′-GCGACTCCGAGCGTGTGCATGATG-3′)[27] was injected into 1-cell stage *Tg(gsc::EGFP-CAAX)* embryos, together with 50 pg of *H2B-mCherry* mRNA to mark cell nuclei. 2 ng of *wnt11f2* MO (5′-GAAAGTTCCTGTATTCTGTCATGTC-3′)[29] was injected into 1-cell stage *MZoep*;*Tg(gsc::EGFP-CAAX)* mutant/transgenic embryos to prevent any potential rescue of the *slb*/*wnt11f2* mutant ppl transplants. 4 ng of human *β-globin* MO (5′-CCTCTTACCTCAGTTACAATTTATA-3′) was used as a standard negative control MO. Induction of ppl progenitors was achieved by injecting 100 pg of *cyc* mRNA.[39]

Interstitial fluid labelling and manipulation of interstitial fluid amount

Interstitial fluid (IF) was labelled by injecting 0.5 nL of 1 mg/mL of Dextran Alexa Fluor 647 (D22914, Invitrogen) between the deep cells (DCs) of high to sphere stage dechorionated embryos using a microinjection needle[4] (3.3–4 h post fertilisation, hpf). In order to increase the IF amount in wild type (wt) or rescue the IF accumulation in Ouabain (O3125, Sigma-Aldrich)-treated embryos, 0.5 nL of 400 mM D-Mannitol, together with the Dextran Alexa Fluor 647 to label the IF (see above), was injected in high to sphere stage embryos.

Ouabain treatments

For inhibiting interstitial fluid (IF) accumulation in zebrafish embryos, embryos were exposed to 1 mM of the specific Na^+/K^+-ATPase inhibitor Ouabain (O3125, Sigma-Aldrich) in standard embryo medium (E3) from 0.5-3.3 hpf, after which the inhibitor was washed off, embryos were dechorionated in E3, and the remaining IF accumulations were labelled as described above (interstitial fluid labelling and manipulation of interstitial fluid amount).

Digitoxin treatments

For inhibiting interstitial fluid (IF) accumulation in zebrafish embryos, embryos were exposed to 10 μM of theNa^+/K^+-ATPase inhibitor Digitoxin (D5878, Sigma-Aldrich, dissolved in dimethylsulfoxide (DMSO)) in standard embryo medium from 0.5-3.3 hpf, after which the inhibitor was washed off, embryos were dechorionated in E3, and the remaining IF accumulations were labelled as described above (interstitial fluid labelling and manipulation of interstitial fluid amount). For control, 1% DMSO was added to E3.

Sample preparation for live imaging

For upright confocal live imaging, embryos were dechorionated, mounted in 0.3%–0.5% low melting point (LMP) agarose (Invitrogen) and placed in custom-made 2% agarose molds. For high-resolution confocal imaging, embryos were mounted in 0.5% LMP agarose on glass bottom dishes (MatTek). Fixed samples were mounted in 0.5%–1% LMP and placed in custom-made 2% agarose molds and imaged on an upright confocal microscope. Live imaging was performed at 28.5°C ± 1°C.

Imaging setups for live and fixed imaging

For confocal imaging of live and fixed samples, Zeiss LSM 880 and 900 upright confocal microscopes equipped with a Zeiss Plan-Apochromat 20x/1.0 water immersion objective were used. Bright-field/fluorescence time-lapse imaging was performed using a Nikon Eclipse inverted wide-field microscope equipped with CFI Plan Fluor ×10/0.3 objective (Nikon) and a fluorescent light source (Lumencor). For high-magnification confocal imaging of prechordal plate progenitors, a Zeiss LSM880 inverted microscope, equipped with a Plan-Apochromat ×40/NA 1.2 water-immersion objective (Zeiss), was used. *In vitro* cell cultures were imaged using a Nikon Ti2E inverted wide-field microscope equipped with Plan Apo λ 20x/0.75 DIC air objective (Nikon) and a fluorescent light source (Lumencor).

Volumetric analysis of gastrulating zebrafish embryos

Data acquisition

For quantifying the interstitial fluid (IF) volume, *Tg(actb2:HRAS-EGFP)* embryos, marking the plasma membrane of all cells, were dechorionated at the 64-cell stage, the yolk cell (yolk) was labelled with 60 μM Nile Red in E3 (20 min at 28°C), and the IF was labelled as described above (interstitial fluid labelling and manipulation of interstitial fluid amount). Embryos were then mounted in glass capillaries (size 4, inner diameter ~2.15 mm) with corresponding Teflon-coated plungers. Matching FEP tube (OD/ID 2.15/1.58 mm) was tightly inserted into the glass capillary. For mounting the sample, an adapted strategy from Kaufmann et al.[46] was used in order to ensure uninterrupted development during imaging: first, ~150 μl of 0.5% LMP agarose containing 1:2000 dilution of fluorescent beads (500 nm, red) was aspirated into the FEP tube using a plunger, after which an embryo was aspirated together with ~300 μM of E3 media, resulting in final LMP agarose concentration of ~0.1–0.2% within the tube. The sample was held vertically until the embryo settled at the lower portion of the FEP tube. Volumetric imaging of gastrulating zebrafish embryos, with the plasma

membrane, IF and yolk labelled, was performed using a Zeiss Lightsheet Z.1 light-sheet microscope, equipped with Plan Apochromat 10x/0.5 water immersion detection and two 5x/0.1 air illumination objectives, in a heating chamber at 28.5°C. Two views (0° and 180°) were acquired, each containing image stacks of 100-120 z-planes at 3-4 μm spacing. The frame rate of the multi-view recording was 3-5 min. For each timepoint and channel, the embryo was illuminated from both sides (dual illumination) and the emitted light was collected at a perpendicular angle. Next, the capillary containing the sample was turned by 180° and the illumination was repeated. Hence, for each timepoint and channel, the dataset consists of 4 views, representing the same embryo from different orientations. The 4 views were reconstructed using the BigStitcher plugin in Fiji.[41,47] The fluorescent beads contained in the sample capillary were then localised and used as reference points for estimating the relative shift between the 4 views. Multi-view reconstruction was performed using these reference points (precise descriptor-based method, default parameters). To exclude imaging artefacts caused by light diffraction due to the opaque yolk structure, a 2x2x2 tiling approach was implemented, resulting in 8 equally sized blocks spanning the embryo. When fusing the 4 views together into one new 3D image stack, for each view only those tiles were included that had sufficient image quality (i.e. the areas of the embryo having the best orientation relative to illumination and detection objective). By selecting tiles for fusion specifically for each view, image slices showing increased light diffraction due to an obstructed light path were excluded. Excluded image slices were then compensated for by selecting the corresponding tiles in another view, thereby including only tiles with good image quality. This approach resulted in enhanced overall image quality of the embryo for all timepoints and channels. The fused dataset comprising all channels and timepoints was down-sampled 4x (in x,y,z) and saved as a.tiff file.

Data analysis

The total embryo volume was computed by segmenting the embryo outline using the expression of HRAS-EGFP labelling the plasma and yolk membranes. Direct thresholding was not possible due to little contrast within the yolk of the embryo. Therefore, a segmentation pipeline based on supervised pixel-classification using the software ilastik[42] (ver. 1.3.3.) was established. Ilastik intensity and texture features computed at three scales (1, 1.6, and 3.5σ) were used to represent each voxel. After interactive labelling of ~5000 foreground (i. e. embryo) and ~2000 background voxels over the entire time range, a Random Forest classifier was trained and used to predict volumetric probability maps for all analysed embryos. The resulting probability maps were smoothed with an isotropic Gaussian filter (3σ) before thresholding at probability 0.5, yielding the initial embryo segmentation. In a few cases, holes in the segmentation were observed in low contrast yolk regions, which were addressed by 3D binary morphological hole-filling to compute the final segmentation. Interstitial fluid volume was computed by segmenting the Alexa647 signal, specifically labelling the interstitial fluid using pixel-classification in ilastik. Intensity and texture features were computed at a wide range of scales and thresholded the resulting maps at probability 0.5, resulting in interstitial fluid segmentation for each time point. Yolk volume was computed by segmenting the yolk cell labelled with Nile Red using the marker-based watershed algorithm. First, a boundary indicator map was computed using Gaussian gradient magnitude with σ ranging from 1.7 to 2.2. This map exhibited high values at the interface of background and embryo, but also between yolk and blastoderm. Next, a small set of voxel markers for background, yolk and blastoderm was defined. Background markers were chosen at the edges of the image stacks and a yolk marker in the centre of the image stack. Markers for the blastoderm were chosen manually from inside the blastoderm with up to 3 distinct marked voxel regions. Then, the watershed algorithm growed all semi-automatically marked voxels spatially in accordance with the supplied boundary indicator map. Low values in the boundary map allowed marker growth, whereas high values in the boundary map inhibited growth. The algorithm stopped when all pixels were either assigned to background, yolk, or blastoderm. All resulting embryo region segmentations were visually inspected. Finally, the resulting segmentations were masked with the embryo segmentation from above to ensure that no voxels outside of the embryo were assigned to either yolk, blastoderm or interstitial fluid. The volume of each region was computed by counting the assigned voxels and multiplication with the according voxel size. All post-processing steps were done with custom Python scripts (ver. 3.8) using the scipy (ver. 1.7.0) and scikit-image libraries (ver. 1.18.1).

qRT-PCR (quantitative real-time PCR)

Wild type (wt) zebrafish embryos (AB background) were collected after laying and half was used as control and the other half was Ouabain-treated from 0.5-3.3 hpf, after which the inhibitor was washed off. Embryos were then dechorionated in E3, and developed until 8 hpf. Total RNA was extracted from 10 embryos per sample using Trizol (Invitrogen). To ensure complete removal of genomic DNA, DNA-free DNA Removal Kit (Thermo Fisher Scientific) was used. cDNA library was generated with the iScript Reverse Transcription Supermix (BIO-RAD) kit according to manufacturer's instructions. The same amounts of mRNA were used from different samples for the qRT-PCR experiment. Experiments were repeated 5x independently in triplicates. Absolute QPCR SYBR Green Mixes (Thermo Scientific) and Bio-Rad C1000 Thermal Cycler was used for qRT-PCR reaction. As negative control, the provided NO-RT Supermix, containing no reverse transcriptase was used. For positive control and normalisation, the housekeeping gene *elongation factor1a* (*ef1α*) was used. To generate the standard curve and determine the linear range, a series of cDNA dilutions were tested to finally use a 1:10 cDNA dilution. The following primers were used at a final concentration of 142 nM: *hgg1* (5' - CTATTATGAGAGAGCAT GTAGCAG - 3' and 5' - CATGTATATGTAGCCTTTGTCAC - 3'), *ef1α* (5' - TCTCTCAATCTTGAAACTTAT - 3' and 5' - AACACCCAGGCG TACTTGAA - 3')

Whole mount immunofluorescence (WMIF)

Embryos were fixed in 4% paraformaldehyde (PFA) overnight at 4°C. After fixation, they were washed in 0.1% Triton X-100 in 1xPBS (PBT) and dechorionated, followed by permeabilization for 1 h in 0.5% PBT and incubation in blocking solution (0.5% Triton X-100, 1% dimethylsulfoxide (DMSO) and 10% goat serum in 1×PBS) for 3 h at RT. Embryos were then incubated with the primary antibody

(rabbit anti-α_1-Na^+/K^+-ATPase [1:1000] or rabbit anti-aPKC and mouse anti-ß-Catenin [1:200 and 1:500]) diluted in the blocking solution overnight at 4 °C, washed 3 x 15 min in 0.1% PBT at RT, and incubated with the secondary antibody (Alexa Fluor 488 goat anti-rabbit or Alexa Fluor 488 goat anti-rabbit and Alexa Fluor 647 goat anti-mouse; 1:1000) diluted in the blocking solution for 3h at RT. Finally, they were washed 3 × 15 min in 0.1% PBT and imaged in 2% agarose molds in PBS using a Zeiss LSM 880 upright confocal microscope equipped with a Zeiss Plan-Apochromat 20x/1.0 water immersion objective.

Analysis of interstitial fluid redistribution centred around the animal-vegetal axis

To track the redistribution of the interstitial fluid (IF) within the blastoderm from 3.5 to 8 hpf, IF was labelled as described above (interstitial fluid labelling and manipulation of interstitial fluid amount) and blastoderm cells were labelled by injection of 1 nL of 1 mg/mL of Dextran-FITC in one-cell stage wild type (wt) embryos. The blastoderm region was then segmented using Ilastik software[42], and used to detect the contour of the blastoderm-yolk cell and blastoderm-EVL boundaries. In addition, IF pockets were segmented using Ilastik software and then binarized in Fiji.[41] To measure the redistribution of IF along the animal-vegetal (AV) axis of the blastoderm, a region of 200 μm width centred around the embryo centre, with the height corresponding to the blastoderm thickness, was predefined. For each time point and a specific position along the AV axis, the binarised IF pixels were summed along the width of the defined region and normalised to the highest value obtained across the entire space and time for each embryo. To indicate the region in which most of the IF resided, 90% IF line was determined by marking the distance from the enveloping layer (EVL)-deep cell (DC) boundary at which 90% of the IF accumulated for each time point. To calculate the IF distribution along the radial axis of the blastoderm at specific time points (4, 6 and 8 hpf as shown in Figures 2B–2D′ and S1B′), the IF distribution was averaged over a 10 min time interval, starting from the time point of interest.

Analysis of interstitial fluid relocalisation at the dorsal side

For quantification of interstitial fluid (IF) distribution on the dorsal side relative to the prechordal plate (ppl) position in either wild type (wt), *slb/wnt11f2* mutant *Tg(gsc::EGFP-CAAX)* embryos, or prechordal plate (ppl) transplanted *MZoep;Tg(gsc::EGFP-CAAX)* untreated or Ouabain-treated embryos, a region-of-interest (ROI) analysis in Fiji[41] was used. The embryos were imaged in a dorsal orientation, and sagittal sections centred around the dorsal side were used for analysis. Initially, IF pockets were segmented using Ilastik software[42] and then binarized in Fiji. The curvature of the embryo was compensated for using the "Straighten" macro in Fiji. IF distribution profiles at the enveloping layer (EVL)-deep cell (DC) and yolk syncytial layer (YSL)-DCl boundary were determined in a region of 20 μm width along the full length of the animal-vegetal (AV) axis and plotted relative to the position of the ppl for 6 and 8 hpf.

Analysis of prechordal plate cell velocity

To characterise the velocity of prechordal plate (ppl) cells in spherical coordinates, all cell nuclei were labelled by injection of 50 pg of *H2A-mCherry* mRNA in 1-cell stage *Tg(gsc::EGFP-CAAX)* embryos marking axial mesendoderm progenitors.[37] The labelled nuclei were then segmented using Imaris (RRID:SCR_007370) software and categorised into enveloping layer (EVL) and ppl cells according to their position on the embryo surface and *gsc::EGFP-CAAX* expression in mesendoderm progenitors. First, the position of EVL cell nuclei was used to determine the radius and the centre of mass of the embryo by fitting a sphere defined by the EVL curvature. The ppl cells were then tracked using Imaris (RRID:SCR_007370) software and their instantaneous velocity (v) was measured over time. To obtain the radial/tangential velocities (v_r/v_θ), the instantaneous velocity of each ppl cell was transformed from cartesian to polar coordinates with the centre of mass of the embryo, calculated as above, as the origin in polar coordinates. The radial/tangential velocities of ppl cells were then averaged over time windows of 3 min. The resultant sum of the radial/tangential velocities were visualised for control (ctrl) and Ouabain-treated embryos.

Cell volume quantification

Surface cell, deep cell (DC), and prechordal plate (ppl) cell volumes were quantified using the Cells algorithm in Imaris (RRID:SCR_007370) software, where cell nuclei and plasma membranes were used to segment individual cells. Pairwise comparisons of not normally distributed data were performed using Mann-Whitney statistical test.

In vitro prechordal plate cell spreading assay

For determining cell spreading *in vitro*, prechordal plate (ppl) progenitors were induced by injecting 100 pg of *cyc* together with 50 pg of *H2A-mCherry* mRNA in 1-cell stage *Tg(gsc::EGFP-CAAX)* embryos. Glass bottom dishes were plasma-cleaned for 2 min and coated with 30 μL of Fibronectin (1:4 in H_2O) per well. When control embryos had reached dome stage (5 hpf), the ppl-induced embryos were transferred and dechorionated on glass dishes in Danieau's medium (58 mM, 0.7 mM KCl, 0.4 mM $MgSO_4$, 0.6 mM $Ca(NO_3)_2$, 5 mM HEPES, pH 7.6). Ppl explants were prepared from ppl-induced embryos by removing the blastoderm from the yolk cell (YC). After YC removal, explants were transferred to glass dishes with pre-warmed DMEM/F12 cell culture medium and cut into pieces consisting of ~50 cells. The explants were then mounted on Fibronectin-coated glass bottom dishes, incubated in culture medium at 28°C for 2h and imaged in respective media using a Nikon Ti2E inverted wide-field microscope equipped with Plan Apo λ 20x/0.75 DIC air objective (Nikon) and a fluorescent light source (Lumencor).

Prechordal plate transplantations

For prechordal plate (ppl) transplantations, *Tg(MZoep;Tg(gsc::EGFP-CAAX))* embryos, lacking all mesendoderm specification and weakly expressing *gsc* to mark their dorsal side, were used as hosts. As donors, wild type (wt) *Tg(gsc::EGFP-CAAX) slb/wnt11f2* mutant embryos, expressing the EGFP in the ppl progenitors, were used either untreated or treated with the Na^+/K^+-ATPase inhibitor Ouabain (1 mM in E3) from 0.5 to 3.3 hpf. At the 1-cell stage, donor embryos were injected with either 50 pg of *H2A-mCherry* or *Life-Act-RFP* mRNA to label the nuclei and actin-rich protrusions, respectively. Depending on the experiment, host embryos were either injected with *wnt11f2* MO (2 ng), or treated with Ouabain (1 mM in E3) from 0.5 to 3.3 hpf to block IF accumulation. After the removal of Ouabain, host embryos were dechorionated, and IF was labelled as described above (interstitial fluid labelling and manipulation of interstitial fluid amount). At 50% epiboly (5.7 hpf), both host and donor embryos were transferred to Danieau's buffer and prepared for transplantation. Using a custom-made transplantation setup (a 20 mL syringe connected to a transplantation needle [ID 20 μm] via silicone tubing), a cluster of ppl cells (10-20 cells) was taken from the ppl of the donor embryos and placed at the yolk syncytial layer (YSL)-deep cell (DC) boundary near the germ margin at the dorsal side of the host embryos. Transplanted host embryos were then mounted for upright and inverted imaging, depending on the experimental assay.

Analysis of radial ectoderm displacement

To characterise the displacement of ectoderm cells overlying the internalising axial mesendoderm on the dorsal side, all cell nuclei were labelled by injection of 50 pg of *H2A-mCherry* mRNA in 1-cell stage *Tg(gsc::EGFP-CAAX)* embryos marking axial mesendoderm progenitors.[37] The labelled nuclei were then segmented using Imaris (RRID:SCR_007370) software and categorised into enveloping layer (EVL), ectoderm, and mesendoderm cells according to their position on the embryo surface and *gsc::EGFP-CAAX* expression in mesendoderm progenitors. First, the position of EVL cell nuclei was used to determine the radius and the centre of mass of the embryo by fitting a sphere defined by the EVL curvature. The ectoderm cells overlying the axial mesendoderm progenitors were then tracked using Imaris (RRID:SCR_007370) software and their position and instantaneous velocity (v) were measured over time. To obtain the radial velocities, the instantaneous velocity of each ectodermal cell nucleus was transformed from cartesian to polar coordinates with the centre of mass of the embryo as the origin in polar coordinates. The radial velocity of ectoderm cells was averaged over bins of 2.5 degrees according to their elevation angle. The resultant sum of the radial velocities over time were visualised in a heatmap. Mesendoderm cells were also tracked over time, and the position of the internalisation site and leading edge (ppl) of these cells was measured from the minimum and maximum values of their elevation angles, respectively. To obtain the radial-velocity distribution of ectoderm cells as a function of their distance to the ppl cells, their radial velocity was averaged over time for bins of equal distance to the leading edge of ppl cells. In the case of *MZoep* embryos, which lack a ppl, the position of wild type (wt) ppl leading edge was used as a reference to calculate the velocity distribution.

Light activation of caged-FITC in the interstitial fluid

Local ultraviolet (UV) laser activation of a caged Dextran, DMNB-caged fluorescein (caged-FITC) (D3310, Molecular probes), within the interstitial fluid (IF) was used to track IF relocalisation. For labelling the IF, embryos were co-injected between the deep cells (DCs) at 3.3-4 hpf with 0.5 nL of a solution containing 1 mg/mL Dextran Alexa Fluor 647 (D22914, Invitrogen) for uniform IF labelling and 1 mg/mL caged-FITC (D3310, Molecular probes) for local uncaging of IF. Injected embryos at 50% epiboly (5.7 hpf) were mounted for upright imaging on a LSM900 upright confocal microscope, and FITC within the IF was locally uncaged using a custom-designed pattern for continuous UV activation. The area of IF accumulation and the rate of accumulation of the uncaged-FITC were quantified at the yolk syncytial layer (YSL)-DC boundary. Fluorescence intensity of uncaged-FITC was quantified against the baseline fluorescence of uniformly distributed IF labelling with Alexa647, controlling for passive diffusion of the uncaged fluorescent tracer. Experiments were performed in wild type (wt) and *MZ*oep mutant embryos, defective in mesendoderm specification. The comparative rate of uncaged-FITC accumulation at the YSL-deep cell boundary for wt and *MZ*oep embryos was acquired by linear regression of raw data.

Yolk cell indentation analysis

To assay the rate of yolk cell indentation as a function of prechordal plate (ppl) internalisation, the yolk cell radius at the germ margin relative to the embryo radius was quantified in wild type (wt) and mesendoderm-deficient *MZ*oep mutant embryos. To generate both of the radii, a disc to the embryo curvature was fitted and the disc centre was detected.

Magnetic tweezer assay

To test whether the pushing force onto the overlying deep cell layer (epiblast) caused by migrating prechordal plate (ppl) would be sufficient to trigger interstitial fluid (IF) relocalisation, a magnetic tweezer assay was performed where a magnetic bead located between the yolk syncytial layer (YSL) and the epiblast was directedly pulled using a localised magnetic field. Mesendoderm-specification defective mutant *MZoep* embryos were kept in standard embryo medium (E3) until high stage (3.3 hpf), after which they were dechorionated and transferred to Danieau's buffer. Magnetic beads (OD 40 μm), conjugated with Streptavidin, were coated with Atto488-biotin for precise localisation within the tissue. Bead implantation was performed at the oblong stage (3.7 hpf). Coated beads were placed within a mineral oil droplet on a glass coverslip for easier access during implantation. Embryos were lined up in a large transplantation mold and oriented laterally. Using a custom-made transplantation setup (a 20 mL syringe connected to a transplantation needle (ID 45 μm) via silicone tubing), several magnetic beads were aspirated and individually implanted into host *MZoep*

embryos. Embryos were incubated at room temperature (RT) for 30 min post-implantation for wound healing, after which the IF was labelled, as described above (interstitial fluid labelling and manipulation of interstitial fluid amount). At 50% epiboly, embryos with correct localisation of the magnetic bead (at the YSL-deep cell/epiblast boundary) were selected for the experiment. The experiment was performed on an inverted Leica SP5 confocal microscope equipped with micropipettes aspiration and magnetic tweezer systems. To prevent it from moving towards the magnetic coil when the magnetic field was switched on, the embryo was held on the yolk cell (YC) side by a blunt micropipette (OD 80 μm/30°), applying a slight aspiration without deforming the surface of the YC. The embryo, with a magnetic bead facing the objective, was oriented laterally, and the bead was pulled in parallel to the animal-vegetal (AV) axis via a locally applied magnetic field during continuous imaging. IF distribution profiles were quantified along the axis of controlled displacement of a magnetic bead following the same method as described above (analysis of interstitial fluid relocalisation at the dorsal side).

Interstitial fluid relocation by micropipette pushing

To determine whether pushing forces applied on the surface of the blastoderm can trigger relocalization of interstitial fluid (IF) from the enveloping layer (EVL)-deep cell (DC) boundary to the yolk syncytial layer (YSL)-DC boundary, a micropipette with an outer diameter of 120 μm was pressed against the EVL in *MZ*oep embryos at 6 hpf where the IF was labelled with Alexa647 as described above (interstitial fluid labelling and manipulation of interstitial fluid amount). IF relocalization was measured around a 15μm z-section around the pipette by segmenting the IF as described above (analysis of interstitial fluid relocalisation at the dorsal side) and determining the fluid fraction. The fluid fraction was measured at the EVL-DC and YSL-DC boundaries to determine the degree of IF relocalisation in response to the applied pushing forces.

QUANTIFICATION AND STATISTICAL ANALYSIS

Graphpad Prism 7 was used for statistical analysis. All data were tested for normal distribution with D'Agostino & Pearson normality test. In case data passed normality test (alpha = 0.05), then a parametric test, such as unpaired t-test or ordinary one-way ANOVA (in the case of multiple comparisons) was used. In case the data did not pass the normality test, a non-parametric Mann-Whitney test was used. The individual statistical tests used for experiments are mentioned in the figure legends. In general, n was considered as the number of independent embryo experiments.